NOAA Technical Memorandum NOS CS 54

A Channel-to-Basin Scale ADCIRC Based Hydrodynamic Unstructured Mesh Model for the US East and Gulf of Mexico Coasts

Silver Spring, Maryland
January 2023

NOAA National Oceanic and Atmospheric Administration

**Office of Coast
Survey National
Ocean Service
National Oceanic and Atmospheric
Administration
US Department of Commerce**

The Office of Coast Survey (OCS) is the Nation's only official chart maker. As the oldest United States scientific organization, dating from 1807, this office has a long history. Today it promotes safe navigation by managing the National Oceanic and Atmospheric Administration's (NOAA) nautical chart and oceanographic data collection and information programs.

There are four components of OCS:

> **The Coast Survey Development Laboratory develops new and efficient techniques to accomplish Coast Survey missions and to produce new and improved products and services for the maritime community and other coastal users.**
>
> **The Marine Chart Division acquires marine navigational data to construct and maintain nautical charts, Coast Pilots, and related marine products for the United States.**
>
> **The Hydrographic Surveys Division directs programs for ship and shore-based hydrographic survey units and conducts general hydrographic survey operations.**
>
> **The Navigational Services Division is the focal point for Coast Survey customer service activities, concentrating predominately on charting issues, fast-response hydrographic surveys, and Coast Pilot updates .**

NOAA Technical Memorandum NOS CS 54

A Channel-to-Basin Scale ADCIRC Based Hydrodynamic Unstructured Mesh Model for the US East and Gulf of Mexico Coasts

Maria Teresa Contreras, Brendan Woods, Coleman Blakely, Damrongsak Wirasaet, Joannes Westerink
University of Notre Dame, Notre Dame, Indiana

Zach Cobell
The Water Institute of the Gulf, Baton Rouge, Louisiana

William Pringle
Argonne National Laboratory, Lemont, Illinois

Saeed Moghimi, Sergey Vinogradov, Edward Myers, Greg Seroka, Michael Lalime, Yuji Funakoshi
Office of Coast Survey, Coast Survey Development Laboratory, Silver Spring, Maryland

Andre Van der Westhuysen, Ali Abdolali
National Centers for Environmental Prediction, College Park, Maryland

Eirik Valseth, Clint Dawson
University of Texas at Austin, Austin, Texas

January 2023

NOAA National Oceanic and Atmospheric Administration

NOTICE

Mention of a commercial company or product does not constitute an endorsement by NOAA. Use for publicity or advertising purposes of information from this publication concerning proprietary products or the tests of such products is not authorized

TABLE OF CONTENTS

LIST OF FIGURES

LIST OF TABLES

ACRONYMS

ADCIRC: Advanced Circulation Model
C-CAP: Coastal Change Analysis Program
CFL: Courant–Friedrichs–Lewy Number
CUSP: Continually Updated Shoreline Project
ECGC: East coast and Gulf of Mexico coast
ESTOFS: Extratropical Surge and Tides Operational Forecast System
FES2014: Finite Element Solution tide model released in 2016
GEBCO: General Bathymetric Chart of the Oceans
GESLA: Global Extreme Sea Level Analysis
GIS: Geographic information system
LEGOS: Laboratoire d'Etudes en Geophysique et Oceanographie Spatiales
MHW: Mean high water
MSL: Mean Sea level
NED: National elevation dataset
NHD: National hydrography dataset
NOAA: National Oceanic and Atmospheric Administration
NCEP: National Centers for Environmental Prediction
NOS: National Ocean Service
UHSLC: University of Hawaii Sea Level Center
USMSL: US Medium resolution shoreline
USGS: US Geological Survey
SRTM: Shuttle Radar Topography Mission digital elevation model
OWI: Oceanweather, INC hindcast wind fields

ABSTRACT

In the context of global warming, inland processes are changing the impact of tropical and extratropical storms, with more precipitation at a higher intensity (Masson-Delmotte et al., 2021; Reidmiller et al., 2018) and lower forward storm speeds (Kossanyin, 2018; Moon et al., 2019). These factors are increasing the vulnerability of large populations living in intercoastal zones, where the hydrodynamics of the ocean interacts with the inland hydrologic processes.

The current Extratropical Surge and Tides Forecast System (ESTOFS) used to estimate water level along the East and Gulf of Mexico Coasts of the US has shown accurate results in the deep ocean and across the shelf; however, its oversimplified representation of the complex nearshore region prevents an adequate representation of the nearshore hydrodynamics and hinders the incorporation of the inland river network.

We used the most recent mesh generation tools to implement a new version of ESTOFS that includes geographic extensions penetrating far into upriver systems up to 10 m above the Mean Sea Level (MSL). This report describes the implementation and validation of the mesh named as the East Coast Gulf of Mexico Coast Model (ECGC) ECGC_120m_2021_v01. The model reduces the minimum resolution from 250 m used in ESTOFS to 120 m and incorporates a significant portion of the inland channels in the nearshore region. In addition, we eliminated over-resolution by considering the overall model cost when designing meshing strategies.

Key Words: Storm surge, astronomical tides, ADCIRC, ESTOFS, modeling, circulation model, water levels, Model ECGC_120m_2021_v01.

1. INTRODUCTION

Coastal interfaces blend processes dominated by upland region hydrology and ocean hydrodynamics (tides, winds, waves, baroclinic fluctuations, among others). These areas tend to be vulnerable to flooding, a matter of concern considering that around 40% of the world's population lives within 100 km of the ocean (Akrofi et al., 2016; NOAA, 2013). In the context of global warming, where future projections indicate more intense and frequent tropical cyclones are expected (Knutson et al., 2010), with slower forward speed (Kossanyin, 2018; Moon et al., 2019), and approximately 20% more precipitation (Masson-Delmotte et al., 2021; Reidmiller et al., 2018), a comprehensive understanding of the multiple risk factors in the coastal regions is more critical than ever.

Specifically in the US, tropical and extratropical cyclones affect the coast every year, being the largest impact natural hazard, resulting in loss of life, severe infrastructure damage, and massive economic losses (Colle et al., 2015; Masters, 2007). With this motivation, the National Ocean Service (NOS) and the National Centers for Environmental Prediction (NCEP) established in 2011 the Extratropical Surge and Tide Forecast System (ESTOFS). This was an effort for integrating astronomical tides as part of the extratropical storm surge modeling system in the Western North Atlantic basin (Funakoshi et al., 2011, 2013) for more accurate water level forecasts during storms.

ESTOFS is driven by the Advanced CIRCulation hydrodynamics model, widely known as ADCIRC (R. A. Luettich et al., 1992; R. Luettich & Westerink, 2004), which has demonstrated accurate prediction for tides and storm surge propagation (Funakoshi et al., 2011, 2013). The model uses an unstructured mesh that allows for the development and propagation of the storm surges from the deep ocean, across the shelf, and into inland coastal waters and across the coastal floodplain. Because the operational run time requirements limited the mesh design, the minimum resolution was constrained to only 250 m, and the total number of nodes to 1.8 million. Additionally, the hand-editing tools used to create the mesh resulted in an unreproducible mesh with sub-optimal resolution distribution, which locates nodes with quasi-uniform resolution in the deep ocean and across the shelf, at the cost of coarser but still uniform size elements along nearshore regions.

The oversimplified representation of nearshore regions has been the main limitation for ESTOFS accuracy in intricate coastal waters and in moving towards models that incorporate components such as rainfall, runoff, and ocean/river interaction. Recent advances (Engwirda, 2014, 2017; Roberts, Pringle, & Westerink, 2019; Roberts, Pringle, Westerink, et al., 2019) now allow for the automatic generation of replicable meshes that optimize the distribution of resolution based on topologic features.

Additionally, recent upgrades in ADCIRC (Pringle et al., 2021) improved the stability and accuracy of simulation using implicit time stepping schemes with larger timesteps. Thus, using ADCIRC v55 significantly reduces the computational cost of simulations, which opens an opportunity for implementing larger meshes that can accurately resolve the complexity of the river network for operational systems.

In this research, we take a first step towards integrating complex dendritic river network as well as coastal inlet hydrodynamics into ESTOFS. We develop a new generation of ESTOFS that incorporates geographic extensions penetrating far upriver systems that convey inland water towards the ocean. We use a combination of the new automatic mesh generation toolboxes to create a modern mesh that efficiently distributes resolution based on topologic features. The model described here reduces the minimum resolution from 250 m used in ESTOFS to 120 m, incorporating a much more significant portion of the channels in the nearshore region. In addition, due to the meshing strategies, over-resolution is eliminated, and overall model computational cost is managed much better.

This report describes the implementation and validation of the model, but not its operational aspects, and we will refer to the mesh described as the East Coast Gulf of Mexico Coast Model **ECGC_120m_2021_v01**. The report is organized as follows: Section 6 describes the general methodology to create an accurate and stable mesh. Sections 7 and 8 present the datasets and criteria used as inputs in the mesh generation. Section 9 shows the implementation of the attributes associated with the mesh for its validation, which is presented in section 10 for tides, and section 11 for historical storms. Finally, section 12 shows conclusions and future work.

2. METHODOLOGY

The keys for developing an accurate, stable, and efficient mesh are the element quality, appropriate element size (resolution), and correct and precise representation of the hydrodynamically relevant topo/bathymetric features. In the nearshore region, where we need to resolve features at much smaller scales than in the deep ocean, a precise alignment of the elements with the wet/dry interface is crucial. This allows us to cleanly represent channels or small islands whose size is similar to the minimum element size permitted in the mesh design.

Figure 1 shows the methodology we use to create the ECGC_120m_2021_v01. We use a high accuracy shoreline to separate the domain into two subdomains: 1) the waterside and 2) the coastal floodplain. We define the waterside to be the open ocean and all connected inland waters, including bays, estuaries, rivers, and channels that lie below a vertical datum at mean high water (MHW). On the other hand, the floodplain is the usually dry region that can potentially flood during storm events.
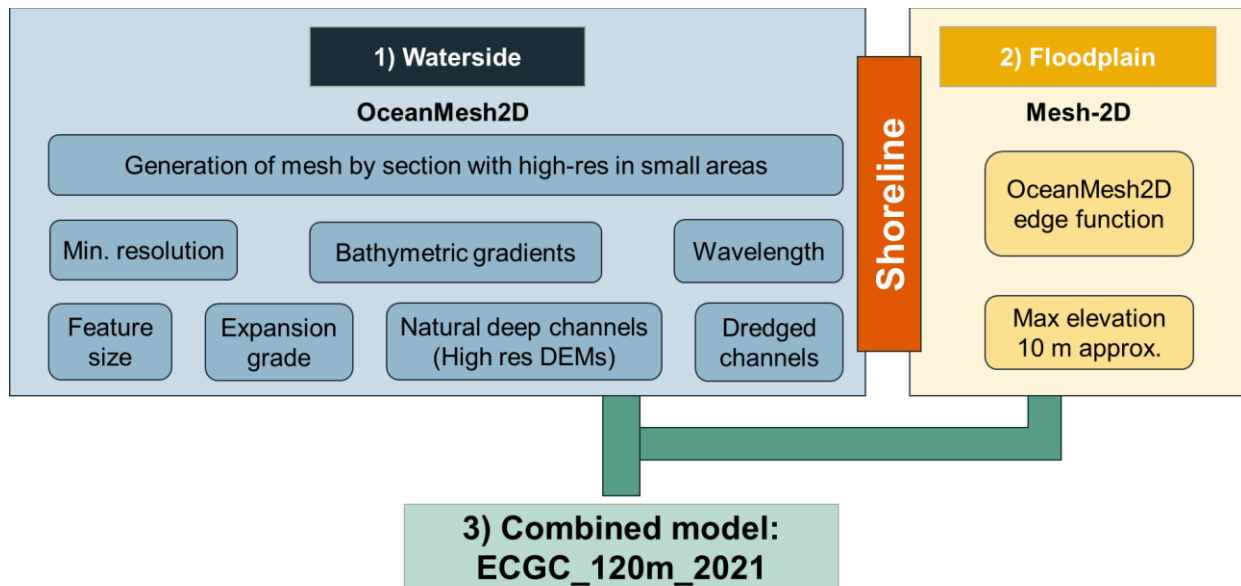
Figure 1: Methodology of the mesh generation: The steps include creating a waterside and floodplain mesh and merging these into one combined mesh. The separation between waterside and floodplain is based on an accurate and continuous shoreline dataset.

We create the mesh in a three-step process; the first two steps consist of generating the waterside mesh first, and then using and constraining the waterside nodes at the shoreline to develop the floodplain mesh. The final model is the result of joining the waterside and floodplain meshes, both having conforming nodes at their interface.

To create the waterside of the mesh, we use OceanMesh2D (Roberts, Pringle, & Westerink, 2019; Roberts, Pringle, Westerink, et al., 2019; Roberts & Pringle, 2018), an automatic MATLAB toolbox to generate and post-process high-quality and

multiscale unstructured meshes for two-dimensional ocean models. One of the main advantages of this tool is having capabilities to incorporate geographic information to define boundaries and zones of interest. Thus, the mesh design is driven by geometric topo-bathymetric features threaded through vector and raster GIS files. Based on these input files and a set of user-defined parameters, the toolbox automatically computes the mesh size function, or so-called edge function, representing a target mesh size criterion (see Figure 1). Some of the criteria that the toolbox uses in this process includes minimum target resolution, bathymetric gradients, the location of natural or dredged deep channels, among others. The toolbox distributes the nodes based on a force balance algorithm, that along with post-processing strategies, improve the overall element quality as well as the worst-case triangle quality. OceanMesh2D generates the mesh by iterating until a convergence criterion based on a combination of target minimum element quality and a maximum number of iterations is achieved.

Once we finalize a stable and tides-validated waterside mesh, we use Mesh2D (Engwirda, 2014, 2017) to create the floodplain mesh. Even though OceanMesh2D has capabilities to generate meshes over the floodplain, the force balance algorithm has difficulties converging to good quality results when constraining nodes for large and complex domains. In the opposite, Mesh2D is another MATLAB toolbox based on Delaunay triangulation, whose main advantage is fixing the position of the nodes at the boundary and within the domain. We select the nodes along the coastline on the waterside mesh and use them to set the location of the boundary nodes of the floodplain. Because the toolbox is not as specialized as OceanMesh2D at defining the element size function based on topology, we use an edge function created with OceanMesh2D following the same criteria as the waterside mesh.

We finally join the ocean mesh and the floodplain by using functionalities included in OceanMesh2D, which preserves the precise delimitation of the wet and dry sections of the mesh. Additional processing, such as incorporating levees, the definition of nodal attributes, and others, is done with OceanMesh2D. Further information about these steps is provided in the following sections.

3. DATABASES

Because the entire mesh design is based on geometric and topo-bathymetric features and their characteristics, having the most accurate datasets to represent the shoreline, the topo-bathymetry, the location of channels, among others, is more relevant than ever. One of the main challenges of resolving topographic features at small spatial scales is the need for higher resolution and higher accuracy databases. In this section, we describe the inputs that we use for OceanMesh2D and Mesh2D to create ECGC_120m_2021_v01.

a) Shoreline

The shoreline is essential for the mesh generation process since it divides the waterside mesh from the floodplain. The NOAA US medium shoreline (USMSL) is the only continuous dataset available for the country's entire East and Gulf of Mexico coasts (NOAA's Ocean Service, 1998). Figure 2 shows examples of the alignment of the USMSL with satellite images at different spatial scales. While frames a and b show a correct representation of the Delaware and Maurice River at scales of kilometers, frame c shows obvious misalignment issues. As we zoom in the scale of hundreds of meters, we notice that the lack of resolution (1:70,000 on average), the constant evolution of the coast, and drift problems often result in misalignments of the shoreline compared with different high-resolution DEMs and satellite images. Consequently, using the USMSL to generate the mesh would result in poor bathymetry, specifically along channels and small topographic features, significantly impacting the model's accuracy in the nearshore region.

The Continually Updated Shoreline Product (CUSP) is a new NOAA database that provides a high-resolution high-accuracy definition of the coastline all along the Atlantic Coast of the US (Aslaksen et al., 2019; NOAA and NGS, 2021). Figure 2d shows an example of the alignment of CUSP when compared with satellite images. The level of detail provided in CUSP, extracted from aerial photos, satellite imagery, and lidar databases at resolutions that vary from 1:1000 to 1:24,000, is enough to represent small-scale features and narrow channels, jetties, groins, and breakwaters (Graham, 2020). Because part of the purpose of developing CUSP is classifying the different uses and structures along the coastline, the database is a discontinuous set of short sections of shoreline. Additionally, during the implementation of ECGC_120m_2021, CUSP has still been under development and does not provide information for the entire domain of interest.

The National Hydrography Dataset (NHD) is a USGS product that provides the most updated representation of the water drainage network in the country (USGS, 2001). While the focus of this database is the definition of inland water bodies, it also offers

information of the coastline at a scale that varies from 1:24,000 to 1:63,360.
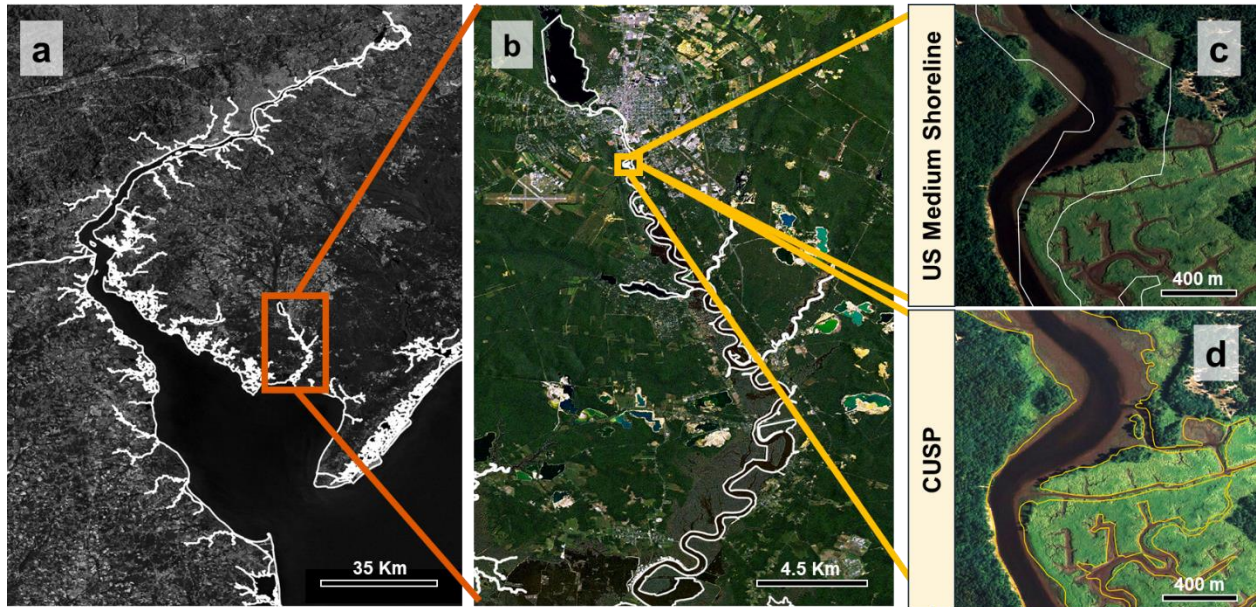
Figure 2: Differences of alignment, at different spatial scales, between the US Medium model and CUSP in the Delaware and Maurice River, NJ.

Because none of the three databases previously described met the need of providing a continuous and accurate representation of the entire U.S East and Gulf of Mexico shorelines, we developed an improved coastline that melds: 1) CUSP wherever it is available, with 2) NHD to fill up the missing gaps, and 3) USMSL where none of the two previous ones were available. Figure 3 shows the coverage of the resulting product with some examples of its accuracy at representing dendritic river networks, deltas, jetties, small islands, etc. The shoreline extends from Maine to Texas at MHW, and we provide it as a continuous line in a shapefile in WGS84 that can be used as input for OceanMesh2D to define the wet/dry interface. Another advantage of this product is it includes delineating rivers farther upstream than CUSP and USMSL, which sets the conditions for incorporating the river network as part of the model for coupling the hydrology in future.
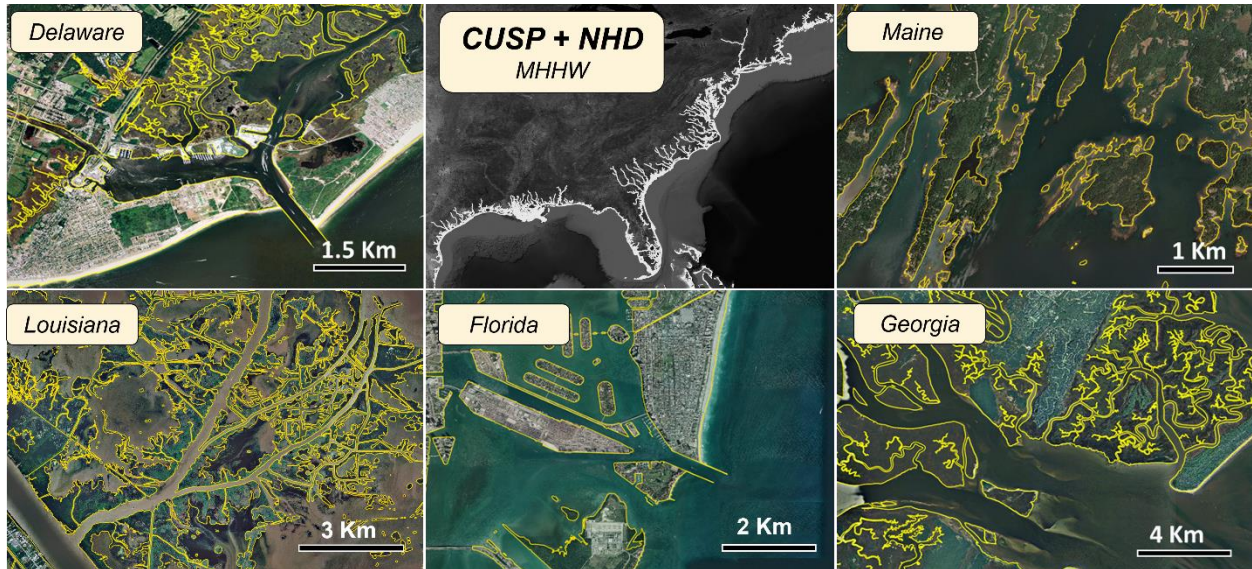
Figure 3: Coverage of the shoreline at MHW that we use to create ECGC_120m_2021, resulting from combining CUSP and NHD in a continuous dataset.

b) *Topo-bathymetry*

As mentioned previously, we use bathymetric databases to define the element size function and to interpolate the topo-bathymetry onto the mesh. Because of the high computational cost of using high-resolution DEMs to define the edge size function and the difficulty of parallelizing the process, we use GEBCO 2019 (Compilation, 2019; Weatherall et al., 2019) for this purpose. However, our smaller experiments show that the difference in the resulting meshes when using higher resolution DEMs to define the edge size function are small mainly because we use the DEMs along with other geographic information (definition of shoreline, location of channels, among others).

However, the water depth values, particularly in highly dissipative areas (ex.: the Gulf of Maine) and nearshore, are the most crucial factor that determines a correct hydrodynamic representation of the system, which forces us to collected a wide set of bathymetric datasets searching for the most accurate values. For the deep ocean, we use GEBCO 2019 with corrections based on SRTM15+V2 (Tozer et al., 2019) around Sable Island. We collected all the publicly available data in the domain for the shallower areas, shown in Figure 4. The DEMs come from USGS, NOAA, USACE, Northeast Ocean Data and are defined at resolutions that vary from 90 to 1 m. We use GDAL to project all the data to the WGS84 coordinate system and VDatum to transform it to the NADV88 vertical datum. We interpolate the waterside of the mesh and the floodplain side of the mesh separately to ensure a clean definition of the wet/dry interface and the conveyance of small-scale channels. The waterside to floodplain interface uses the waterside value.

7

We use a element-averaged approach to interpolate the values at each node: we average all the DEM values within a window whose size is the mean of the resolution of the elements connected to the node. We only use nodes with positive water depth in the DEMs to interpolate the waterside, ensuring the bathymetry of small channels is not dry due to the averaging with surrounding topography. On the floodplain side, we only use floodplain values to define topography and do not average in adjacent waterside values. Additionally, we enforce a minimum water depth of 30 cm on the waterside and 10 cm above sea level on the floodplain, ensuring a smoother gradient transition between the waterside and floodplain, ensuring that elements inundate and drain smoothly.

Because the multiple datasets overlap at different regions, we interpolate by layers, starting with the coarsest DEMs, and overwrite the values based on the most accurate dataset. Thus, we first interpolate GEBCO2019 on the waterside and NED on the floodplain. We then continue with the order of layers shown in Figure 4, ensuring we preserve the most accurate data and reduce the possibility of areas with no data values.

After interpolating the large DEMs shown in Figure 4, we focus on locally fixing the bathymetry of dredged channels and rivers. To do so, we use the USACE Dredged channels database (USACE, 2021-b) and NOAA charts (NOAA Office of Coast Survey, 2021) only in areas where the DEMs clearly have incorrect bathymetric values (see Figure 5). Notice that wherever the USACE dredged channels database provides DEMs based on surveys, we use GDAL and VDatum to transform them to WGS84 and NADV88, so we could directly interpolate them onto the mesh. In cases where there is no survey based DEMs values along designated dredged channels, we interpolate the constant design water depth within the polygon defined in the database. In the case of NOAA charts, we transform the original contour lines to DEMs using the QGIS's built-in Rasterize tool. It is also important to mention that the NOAA charts only provide water depth values, which might introduce errors in the slope of rivers in steep topographic regions or where river bottoms lie above sea level. Because of the flat topography of most of the East and Gulf of Mexico coasts of the US, we observe that this is not in general an issue, although it may introduce bathymetric errors in the region between the Gulf of Maine and Massachusetts.
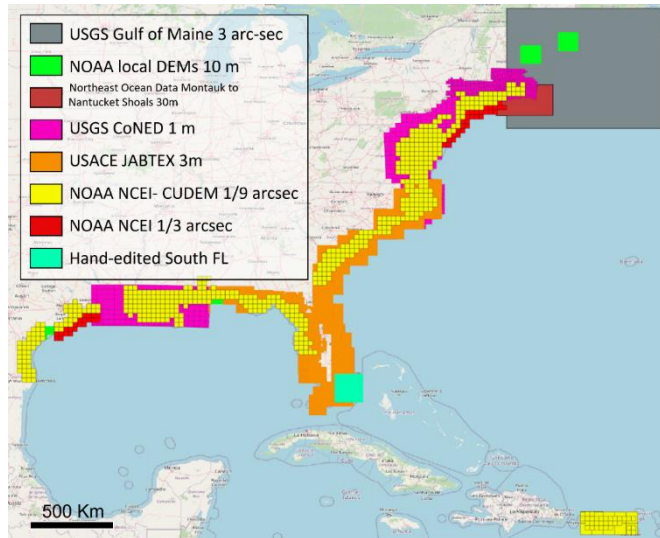
Figure 4: Topo-bathymetric datasets used in the interpolation of ocean and floodplain of ECGC_120m_2021_v01.
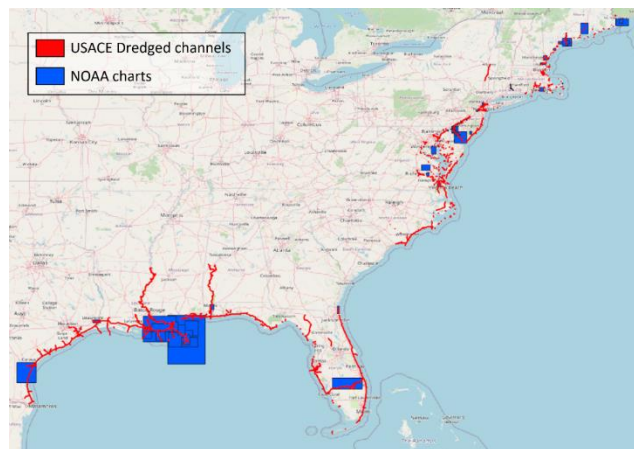
Figure 5: Coverage of NOAA nautical charts and USACE dredged channels databases, both used to correct bathymetry of man-maintained channels and upper sections of rivers.

c) Natural Channels

Natural deep and narrow channels transport a significant part of the flows from/towards the ocean (Dronkers, 1986). One example is the Delaware Bay that has a two-layers estuarine residual circulation pattern, with fresh water flowing to the ocean in the surface, and saline water penetrating the estuary from the shelf in the bottom layers, particularly along these deep channels (Galperin & Mellor, 1990).

The only way to provide an accurate representation of conveyance is by providing sufficient resolution across the channels and interpolating accurate bathymetry (Greenberg et al., 2007; Molines et al., 1989). OceanMesh2D allows for this option when the user provides a set of polylines that define the location of these deep

9

channels. For this purpose, we created a database of thalwegs along the coast by running standard hydrologic routines in QGIS for drainage network extraction over 30 m resolution DEMs result of resampling the high-resolution DEMs in Figure 4. In the deep ocean we directly used GEBCO2019. We hand-cleaned the lines by comparing them with the original DEMs and clipped them at approximately the edge of the outer shelf. Figure 6 shows the extension of the dataset with a zoom in the Delaware Bay.
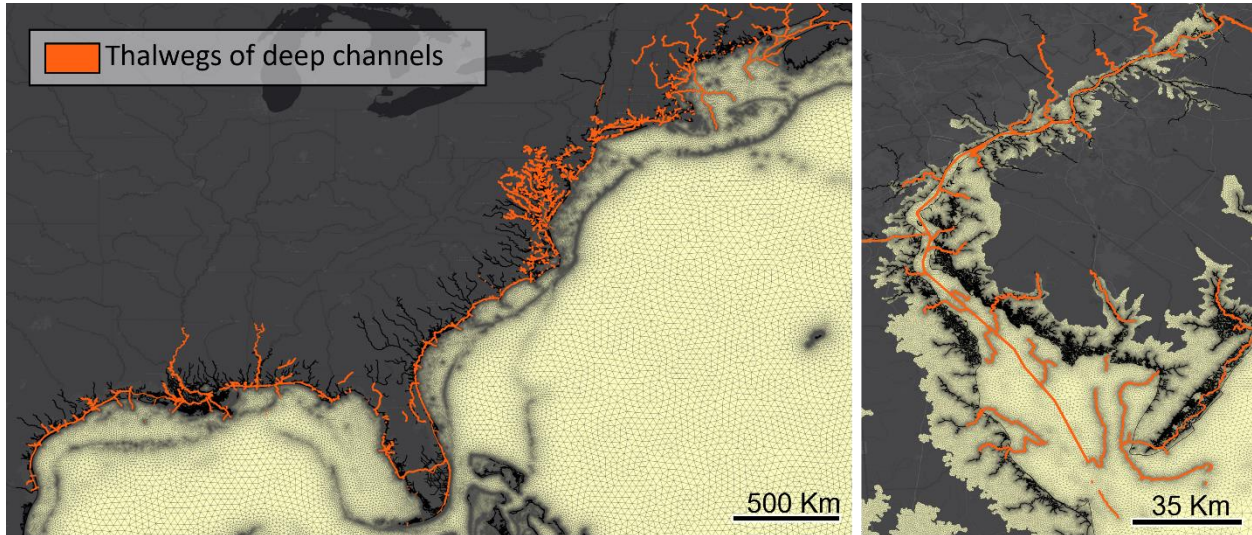
Figure 6: Thalwegs of deep channels extracted with hydrological network methodology from high-resolution DEMs. Example of the higher resolution along the thalwegs in the Delaware Bay.

d) USACE Dredged Channels

The U.S. Army Corps of Engineers (USACE) dredged channels are narrow man-maintained watercourses that span from inlets through estuaries and often into inland navigable channel systems. Typically, these channels are not represented in the DEMs. Like the natural deep channels, they also need high resolution to model their deepest portion properly. We use the USACE Dredged channels database (USACE, 2021-b; *USACE Hydrographic Surveys*, 2021), shown in Figure 7 to characterize them. The database provides polygons with the design water depths, and for some regions, there are survey based DEMs. After transforming all the data to WGS84 and NAVD88, we computed the centerlines of the polygons. We used them in the waterside generation, together with the thalwegs of deep natural channels, to provide higher resolution. We also used the available DEMs or design water depths to correct the bathymetry along these dredged channels as described in section 7b.

10
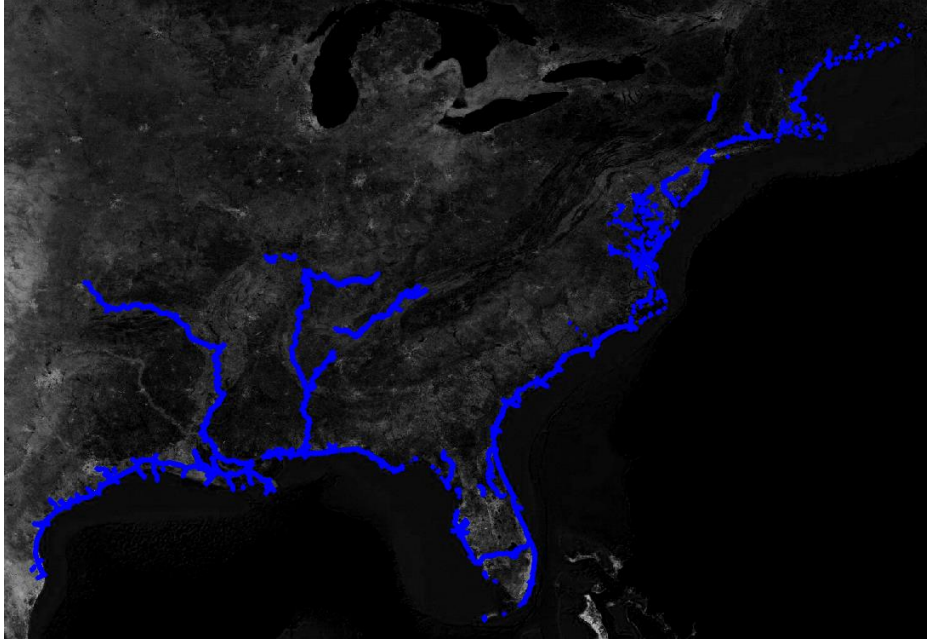
Figure 7: Coverage of the USACE dredged channels database.

4. MESH DESIGN

As we mentioned in section 6, we created the mesh in a three-step process, generating the waterside and floodplain separately, and combining them into the final product. Figure 8 shows an example of the two subdomains and the combined model. The images illustrate the complex riverine network and the small scale bathymetric/topographic features in the model achieved by aligning the nodes along the coastline. Additionally, frame c shows the exact match between the boundary nodes on both water and floodplain subdomains, with a zoom in frame d, facilitating the merging process.
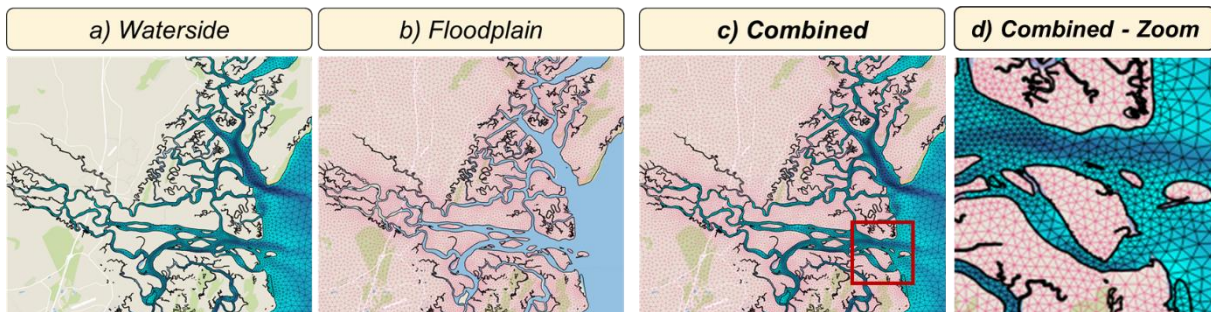
Figure 8: Differentiation of the ocean side and floodplain in ECGC_120m_2021_v01.

We calibrated the OceanMesh2D mesh generation parameters to define the distribution of nodes, so we can create a stable and accurate model with smooth transitions between different resolutions that incorporate the riverine system to the extent possible given the target minimum resolution associated with operational run time constraints. As shown in Figure 1, we used OceanMesh2D to define the element size function for both the ocean and floodplain. Table 1 shows the values of the parameters we use for each section. With the minimum resolution, we determine the minimum edge length allowed in the grid. On the other hand, the maximum resolution is constrained by a combination of the value nearshore ($0.1°$ from the shoreline) and over the entire domain.

The geographic information near the coast plays an important role in determining the resolution through the combination of the feature size function and the expansion grade. While the first one analyzes the width of two-dimensional features using the medial axis as a reference to determine the "complexity" of the coastline, the second one constrains the maximum gradient of the element size to ensure smoothness of the nodal distribution. With the slope, we provide extra resolution along steep topo-bathymetric gradients, such as shelf break and submarine ridges. Similarly, we use the locations of channels, defined as polylines, to provide extra resolution along dredged channels and submerged river basins that often are not captured by the

slope or feature size. In the deep ocean, the two most relevant parameters are the wavelength and Rossby radius filter. While the first one provides extra resolution to make sure there is a minimum number of nodes along a M_2 tidal wavelength, the Rossby deformation filter reduces resolution by cleaning concentrations of nodes due to noise bathymetry. For a further detailed description of the mesh generation parameters, refer to Roberts & Pringle, 2018 and Roberts, Pringle, & Westerink, 2019.

Table 1: Parameters used to define the edge size function for ECGC_120m_2021_v01.

Parameter	Deep Ocean	Shallow Water	Floodplain
Minimum resolution $[m]$	1000	120	120
Maximum resolution nearshore $[m]$	-	250	250
Feature Size $[-]$	2	2	2
Expansion grade $[-]$	0.2	0.18	0.12
Slope $[-]$	20	20	20
Rossby radius filter $[-]$	-30	-30	-30
Channels $[-]$	0.1	0.1	0.1
Wavelength $[-]$	100	100	-
Maximum resolution $[m]$	24,000	24,000	500

Because of the difference in the spatial scales of the features that we resolve in the deep ocean and the nearshore region, we separated the waterside mesh into two regions, the deep ocean and the shallow water where we provide more resolution. Thus, the resolution varies from 1 to 24 Km, with a 20% expansion grade in deep waters, while it changes from 120 to 250 m along the shoreline with an 18% expansion in shallower nearshore, inshore and inner shelf waters.

Defining the element size function involves many controls beyond the expansion grade. In the deep ocean, we constrain the maximum element size depending on the major tidal constituents' wavelength and adequately solve the significant bathymetric gradients. We limited the maximum element size to a minimum of 100 nodes per M_2 wavelength. We also use the slope parameter, which is particularly relevant for solving the deep ocean's internal tide dissipation, changes in the celerity of the waves, and reflective effects of tides and surge off the continental shelf break which can reflect back nonlinearly generated tides as well as storm surges. Figure 9a shows examples of the higher resolution along the inner continental shelf and regions with steep bathymetric gradients. Since the bathymetric gradients such as those associated with underwater mountains can introduce clusters of nodes in regions with no significant changes in the ocean's hydrodynamics, we use a filter based on the Rossby radius of deformation.

In shallow shoreline and inland regions, the feature size function distributes resolution based on the width and the complexity of 2D features using the distance from the medial axis and the directionality of the medial axis. Because this can be considered a measure of the complexity of the shoreline, it provides more resolution wherever there are narrow channels, small islands, and complex curvatures of the shoreline (see Figure 9b).
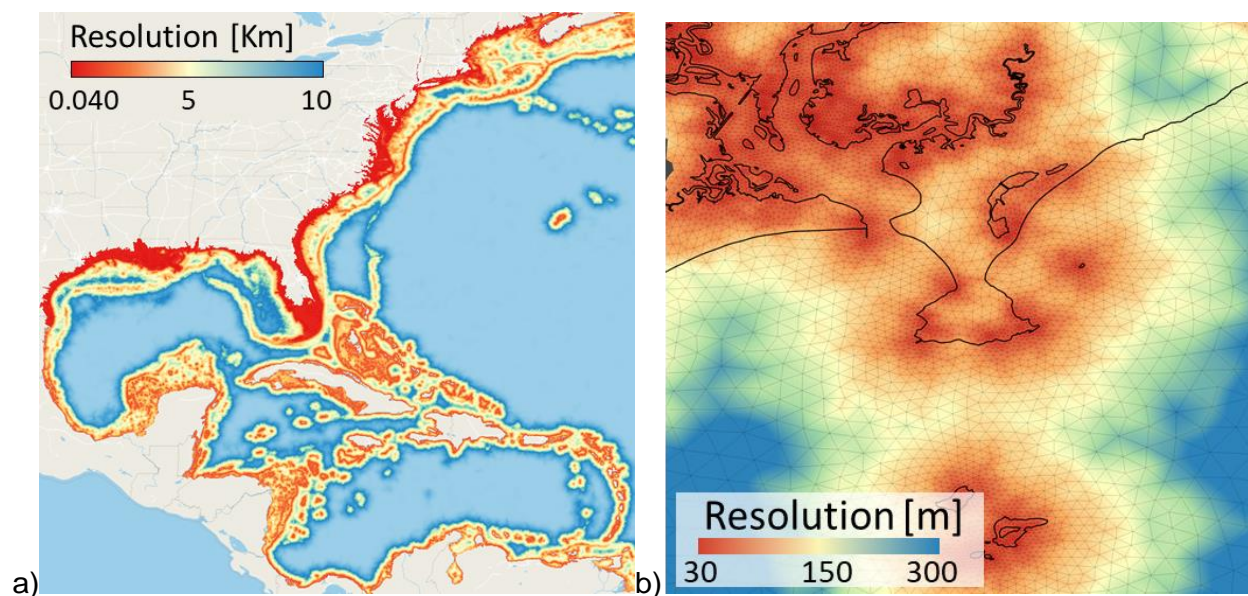
Figure 9: Distribution of the resolution in ECGC_120m_2021_v01. A) Highly resolved areas include the floodplain, shoreline, shelf, Gulf of Maine, and Bay of Fundy. B) Example of higher resolution in sections of the shoreline with complex topographic features.

We also use the channel parameter to provide additional resolution along natural deep and dredged channels, both characterized by being particularly narrow and deep. Figure 10 shows that by specifying the location of these channels (Figure 10a) using databases described in sections 7c and 7d, we increase the resolution (Figure 10b) to represent better the deepest portions of the channels (Figure 10c) and to preserve their shape and conveyance.
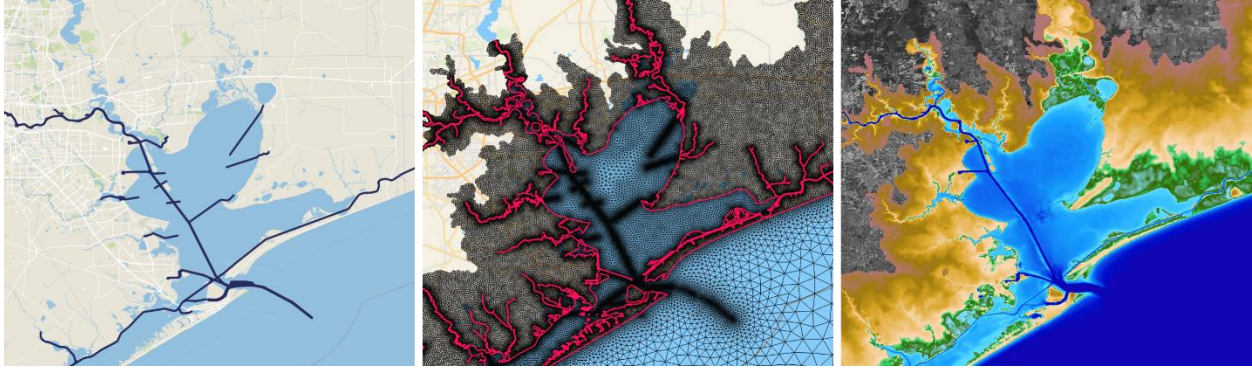
Figure 10: Different uses of the dredged channels dataset in the Galveston Bay. From left to right, the images show: a) The USACE dredged channels dataset, b) Higher resolution along the centerlines of the waterways, and c) Bathymetric interpolation to preserve open watercourses.

Across the floodplain, we use a resolution that varies from 120 to 500 m with a 12% expansion grade. For this region, we keep the parameters that assign extra resolution to topographic gradients and the complexity of the shoreline from the waterside, so the element size function has a smooth transition across the wet/dry interface. We extended the floodplain to approximately 10 m above sea level, using a simplified contour line extracted from GEBCO 2019.

With this configuration, we merge the waterside and floodplain, creating ECGC_120m_2021_v01 with 6,091,419 nodes and 12,039,738 elements covering a domain from 7.9 to 45.86 N and 60.00 to 98.01 W. The high-resolution and floodplain extend along the US East and Gulf of Mexico Coast from the border with Canada into the Gulf of Maine to the border with Mexico in south Texas.

5. MODEL IMPLEMENTATION

After merging the waterside and floodplain, we must assign a series of attributes to complete the description of the physical system in the model. First, we must specify elevation boundary conditions along the open ocean boundary shown in Figure 11. The open Atlantic Ocean boundary located at 60.00 W and forcing tides are based on the TPXO9 data assimilated global tidal constituent database (Egbert & Erofeeva, 2002). No normal flow land boundary conditions are specified along land and island boundaries as well as along the upper limit of the floodplain. Additionally, we incorporated the levee systems located around the Mississippi River and vicinity in Louisiana. We describe the levee database and implementation in section 9a. Additionally, we use a subgrid barrier island feature described in section 9b to hydrodynamically represent the barrier islands meshed with only one element across. In terms of dissipation, we specify bottom friction and internal tides dissipation, whose parameterization is described in section 9c. Time stepping is summarized in section 9d.
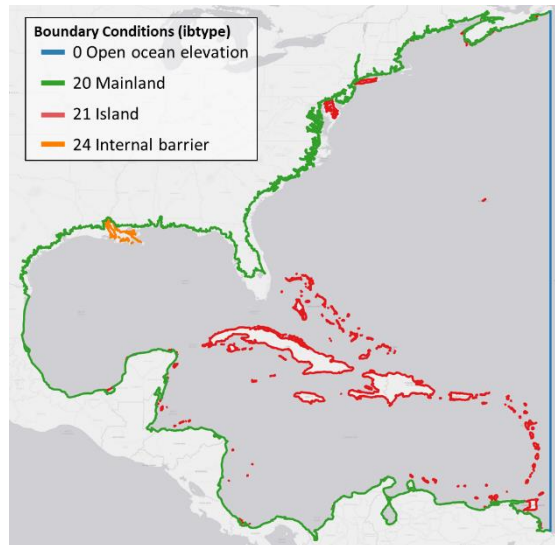
Figure 11: Boundary conditions defined in ECGC_120m_2021_v01.

a) *Incorporation of levees systems*

The levee systems in the Mississippi River area are crucial to correctly estimating water levels and flooded areas during storms. We use the USACE levees database (USACE, 2014), a database of surveyed points that define the location and elevation of these structures. Figure 12a shows an example of the database in St Charles Parish, LA. As the image shows, levees are structures usually built along the boundary of water bodies, coinciding with the location of the wet/dry interface. We snapped the levees to the nodes along the waterside mesh boundary at all the

17

sections where the levee was close enough to the wet/dry interface. We resampled the remaining sections with nodes distanced by approximately the target element size and fixed the location of those nodes during the generation of the floodplain. Figure 12b shows how we preserve a precise definition of the levees that match the original database.
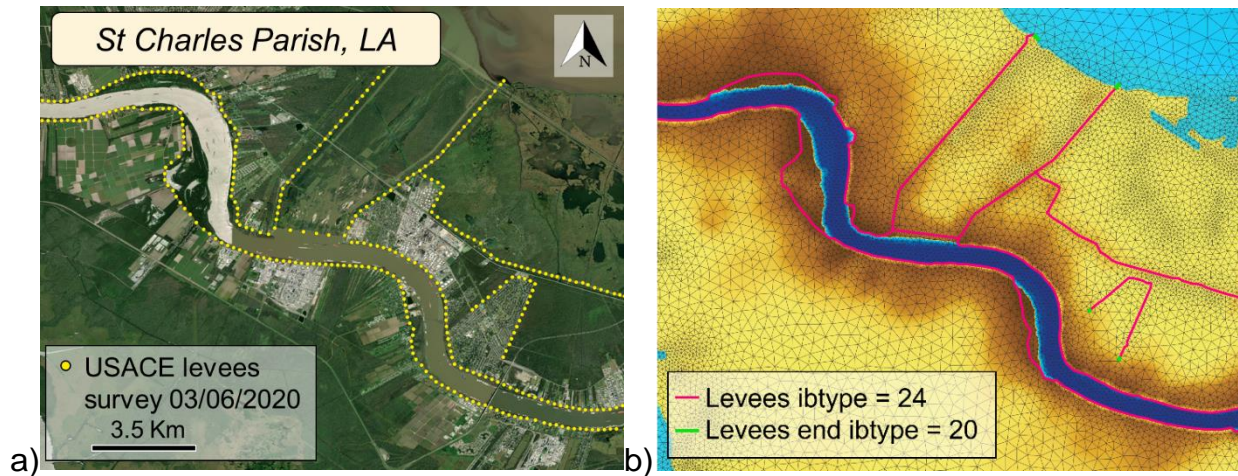
Figure 12: Example of the levees a) database, and b) their representation in ECGC_120m_2021_v01.

Representing levees as weir boundary conditions in ADCIRC requires pairs of nodes disconnected in the triangulation but paired through the boundary condition. While levee pairs have typically been specified with a finite distance between them, we add an infinitesimally thin pairing option to ADCIRC V56 to facilitate merging water and land meshes as well as to eliminate undersized elements at the ends of levees. Thus, after aligning nodes with the location of the levees and merging waterside and floodplain into a combined mesh, we modified the triangulation of the model, duplicating the levee nodes and changing the connectivity table, so elements on both sides of the levees do not share nodes. As a result, we represent the levees as infinitesimally narrow gaps, with paired nodes through the weir boundary condition (IBTYPE = 24, see Figure 11). We also adjusted the levee nodes' bathymetry, ensuring that nodes coinciding with the wet/dry interface preserve positive water depth at one side of the structure and appropriate elevations, typically above sea level, at the opposite side. Finally, to ensure numerical robustness, we ensure that the levee crest elevation is at least 20 cm above the adjacent topography. In cases where the difference was smaller than 20 cm, we corrected it by increasing the structure's height. Figure 13 shows in magenta lines the entire federal levees system included in ECGC_120m_2021_v01.
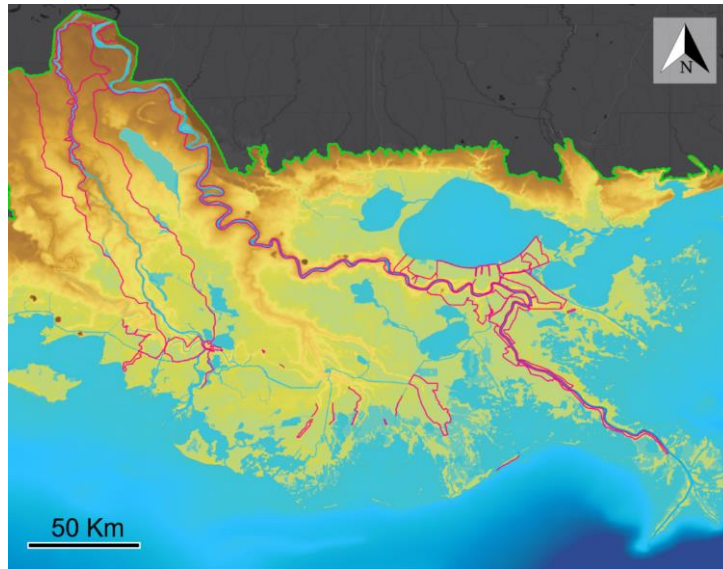
Figure 13: Federal levees implemented as weir boundary conditions in ECGC_120m_2021_v01.

b) Subgrid barrier

The subgrid barrier is a new attribute in ADCIRCv56 that corrects the simulation of thin barrier islands. The resolution distribution, which saves nodes along straight sections of the shoreline, often results in barrier islands represented by one element across. During the bathymetric interpolation, the nodes representing these sections of land have positive water depths, submerging the barrier island elements in the model. This situation is particularly relevant, but not exclusive, to Long Island (NY) and Pamlico Sound (NC). We use the subgrid barrier feature to incorporate their hydrodynamic blocking effect in the model without adding extra resolution in the mesh.

Figure 14 shows an example of a barrier island in Cape Lookout, NC, where we use the subgrid barrier feature. The satellite image on the left demonstrates that even though the barrier island narrows, it is a continuous structure that stops the propagation of tides and waves from the deep ocean to the back bays. Instead, the right-side panel shows that in ECGC_120m_2021, sections of the barrier islands do not have a central node with elevation above sea level, opening the element to free flow from offshore. We select all the nodes representing these structures, see magenta points in Figure 14, and use them as a nodal attribute with an associated elevation based on the topography/crest elevation of these landforms within the element. Thus, ADCIRC interprets that the barrier island elements must remain dry if the water elevation does not exceed the nodal attributes' specified elevation.

The feature is implemented in ADCIRC by leveraging the wet/dry state of the element that would receive cross-barrier flow. Nodal mesh elevations are specified as the bathymetric values rather than the barrier island values, and subgrid barrier attribute data within the nodal attribute file represents the barrier crest elevations. When all overtopping elevations for a given mesh element are exceeded, the bathymetric depth is updated to the barrier island elevation and the restrictions on element wetting/drying are lifted. This allows overtopping to occur normally via the shallow water equations. When the water surface elevation falls below the overtopping elevations, the restrictions on wetting and drying are put back in place and the nodal elevations are returned to the bathymetric depths to allow lateral flows to continue, but overtopping flows to cease.
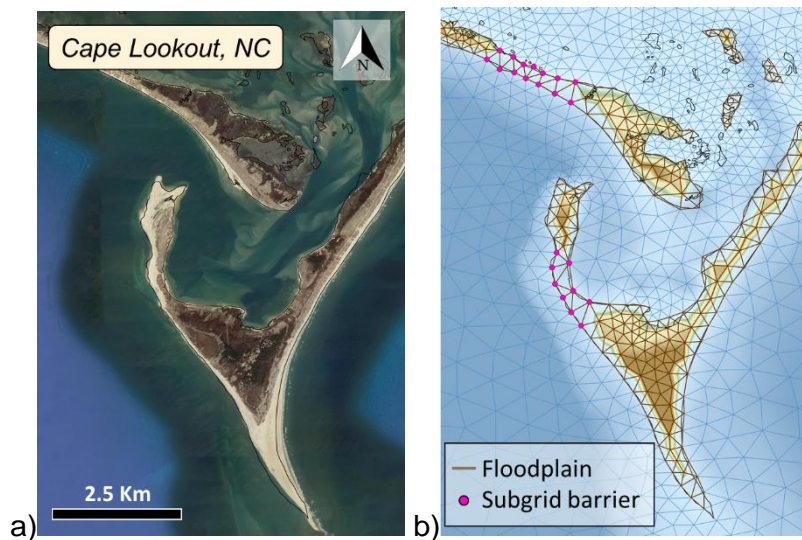
Figure 14: Example subgrid barrier feature in Cape Lookout, NC. Panel a) shows a satellite image of the barrier island, and b) the representation of the land feature in the model, with the selected nodes used in the subgrid barrier nodal attribute.

c) Dissipation parameters

The bottom boundary layer and internal tides are the two primary dissipation mechanisms in coastal ocean modeling, and both are included in ECGC_120m_2021_v01.

The bottom friction is parameterized through the Manning coefficients shown in Figure 15. In the ocean, we use 0.022 as the default value. We added polygons for higher Manning values based on high-dissipative areas and lower friction values in regions with uniform underpredictions on initial tidal simulations. The values shown in Figure 15 resulted from trial and error, optimizing the results for the amplitude of the M_2 tidal constituent when comparing results against a set of 792 gauges. More details about the tidal validation are presented in section 10.

Area	Manning n
Deep Ocean	0.022
Bay of Fundy	0.028
Gulf of Maine	0.032
Long Island	0.028
Delaware Bay	0.023
Chesapeake Bay	0.019
West Florida	0.029
Gulf of Mexico	0.012
Caribbean	0.028
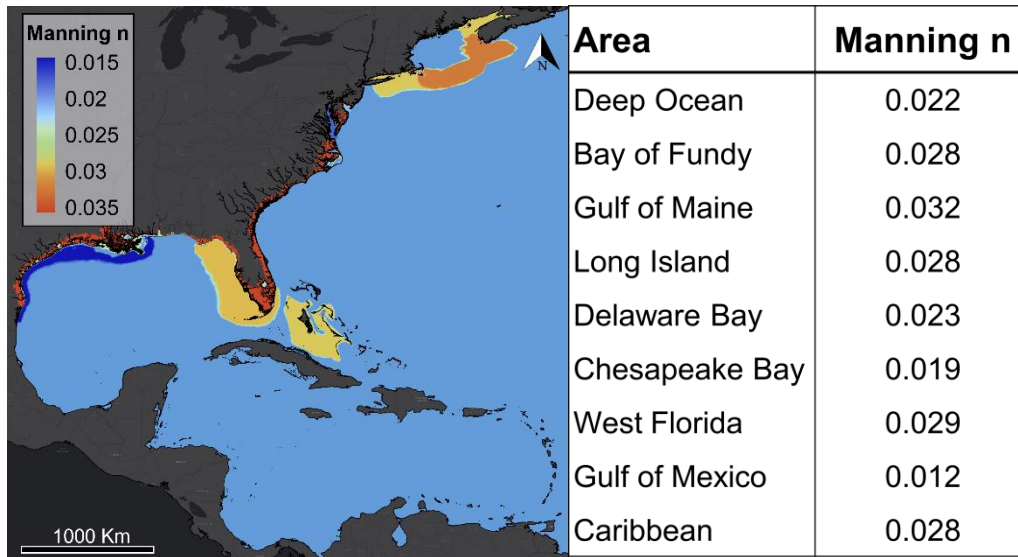
Figure 15: Manning coefficients for calculating the bottom friction dissipation in ECGC_120m_2021_v01.

We interpolated the friction coefficients in the floodplain based on data from the NOAA C-CAP Regional Land Cover database from 2016 (*C-CAP Regional Land Cover and Change*, 2016). We use the nearest neighbor interpolation method for all nodes whose water depth was 4 m or above. Figure 16 shows three examples of the Manning values overland in South Florida, Louisiana, and Texas.
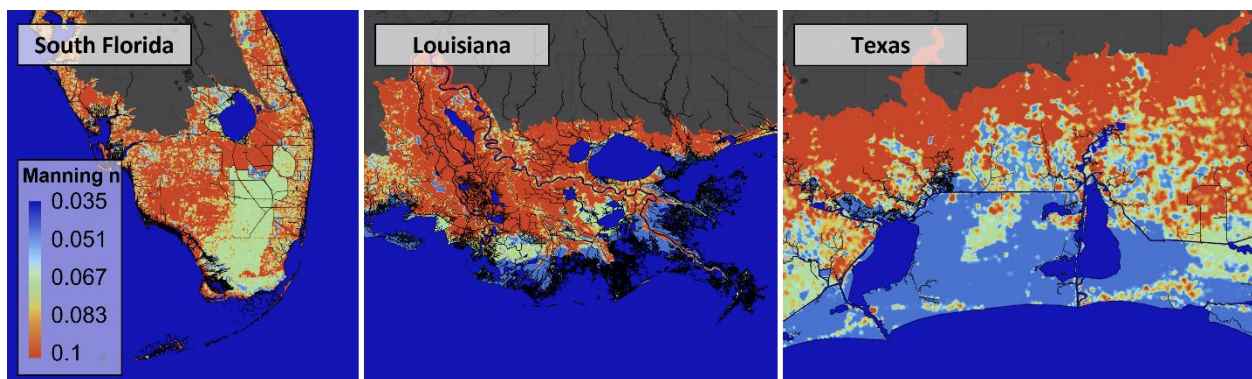
Figure 16: Examples of the overland Manning values in South Florida, Louisiana, and Texas (from left to right).

ADCIRC transforms the Manning n values to the equivalent quadratic friction coefficients to compute the bottom layer friction momentum losses. In this transformation, the deep ocean can result in unrealistically low friction coefficients. We limited the quadratic friction coefficients to a minimum of 0.0005.

For the internal tides, we use the directional parametrization defined in Pringle et al.,

21

2018, which depends on the local bathymetric slopes and a dimensionless scale factor. We computed the bathymetric gradients directly from the DEMs shown in Figure 4, considering the average root mean square of the elevation differences within each element for all the elements attached to a node. We use a 2.75 scale factor, as recommended in literature (Pringle et al., 2018), and 250 m cutoff water depth, understanding that in shallower regions the water column is well-mixed. Figure 17 shows the distribution of the internal tide coefficients, where we can observe high values particularly along the continental shelf and steep bathymetric gradients in the Caribbean.
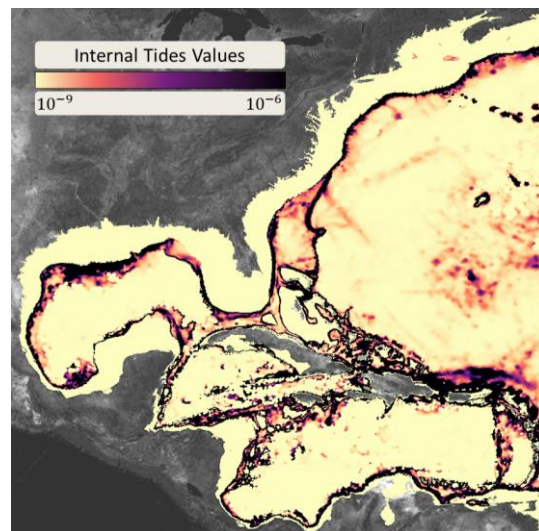
Figure 17: Internal tide factors used in ECGC_120m_2021_v01.

d) *Time stepping*

The mesh is designed to run with a 2 seconds timestep using an explicit time-integration scheme, equivalent to a Courant–Friedrichs–Lewy (CFL) number of approximately 0.2 but this can be increased to 6 seconds using the implicit time stepping settings (Pringle et al., 2021).

In terms of nodal attributes, we use values of the primitive weighting factor in the continuity equation variable in space and time, following the guidelines for ADCIRC (Luettich & Westerink, 2018).

6. TIDE VALIDATION

We ran ECGC_120m_2021_v01 with tidal forcing only in order to analyze its performance in terms of stability and accuracy. We forced the eight predominant constituents (M_2, S_2, N_2, K_1, O_1, P_1, Q_1, K_2) on the open ocean boundary with the data assimilated TPXO9 model database as well as through the tidal potential terms. Amplitude and phase factors were applied. We also included the self-attraction and loading terms based on the FES2014 dataset developed by the Laboratoire d'Etudes en Geophysique et Oceanographie Spatiales (LEGOS). We ran the simulation using the explicit time integration scheme with a 2 second time step. We simulated 75 days, considering ten ramp days and the 65 remaining ones for result analyses. The simulation completed in 22 hours and 17 minutes using 1008 processors. We validated the results against 792 tidal gauges, including LEGOS, NOAA, GESLA, and UHSLC stations.

Figure 18 shows the comparisons of harmonically decomposed results for the eight major tidal constituents. The left panel of each image shows the spatial distribution of the gauges colored based on the magnitude of the error when compared with measured amplitudes. The right-side panel shows the scatter plot comparing in the x-axis the observed amplitudes versus the modeled values in the y-axis. We analyze the results as a combination of relative and absolute error, considering that some of the constituents have amplitudes so small that absolute errors on the order of millimeters can be equivalent to over 50% relative error. Additionally, Table 2 summarizes the statistics for each tidal constituent. In the table, we show the coefficient of determination or R^2, the slope of the trend line y, the standard deviation σ, the mean and absolute mean errors, $\underline{\epsilon}$ and $|\epsilon|$ respectively, and the normalized root mean square error E. In general, we observe accurate computations of the tidal amplitude for all the constituents. The model performs exceptionally well in the deep ocean and shelf, with 100% of the gauges with relative and absolute errors lower than 10% or 2 cm, respectively. In the shallow waters and nearshore region, we expect more significant errors because of the tidal amplification, poor bathymetry, and/or insufficient spatial resolution. In general, we observe good results in most of the domain with very localized problems.

Specifically, the M_2 constituent has the largest mean and absolute mean error, with 0.392 and 2.569 cm, respectively, which is small considering the amplitude of this constituent is up to 3 m in areas like the Bay of Fundy and Gulf of Maine. The R-squared and the normalized root mean square for this constituent are 0.985 and 0.09, respectively, which also indicate an excellent prediction of the predominant tidal constituent. The rest of the constituents have R-squared between 0.65 and 0.98, with the smaller constituents having larger error metrics. Similarly, the normalized root mean square varies from 0.106 to 0.301, somewhat larger than the M_2 constituent.

Even though these parameters may show poorer adjustment of the results for other constituents than the M2, their amplitudes are significantly smaller. Thus, the absolute mean error is less than a centimeter for 6 out of the seven remaining constituents. Only K1 has an absolute mean error of 1.189 cm, which results from the underprediction of the K1 amplitude in the Gulf of Maine (see Figure 18). Because this constituent has notably large errors at deep water stations near the northeast open ocean boundary and because we do not observe this problem in global models with similar regional configurations of the East and Gulf of Mexico coasts, we believe the error is caused by the tidal forcing along the open ocean elevation boundary condition. More detailed analyses in this regard are being performed in ongoing investigations.
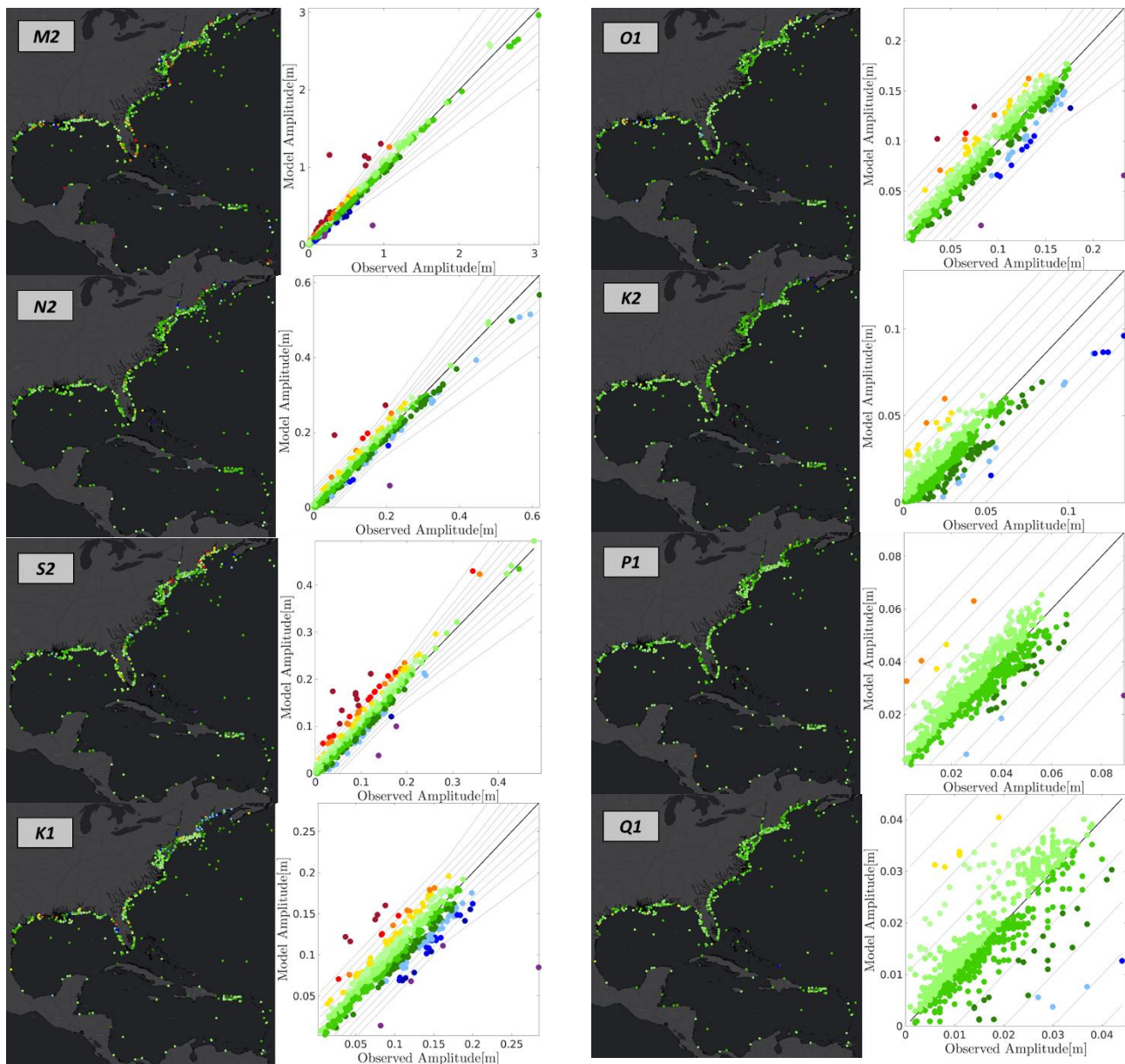
| Abs. Err [cm]: | −5 | −3 | −1 | 0 | +1 | +3 | +5 |
| Rel. Err [%]: | −40 | −20 | −5 | 0 | +5 | +20 | +40 |

Figure 18: Error amplitude for the M2 constituent. The statistics are computed based on comparing the results against 792 stations in the deep ocean, shelf, and nearshore.

Table 2: Summary of statistics when comparing modeled tidal amplitude against a set of 792 gauges.

	$M2$	$N2$	$S2$	$K1$	$O1$	$K2$	$P1$	$Q1$
$R^2 \, [-]$	0.985	0.980	0.953	0.817	0.910	0.816	0.744	0.650
$y \, [-]$	0.999	0.961	1.032	0.979	0.991	0.894	0.994	1.005
$\sigma \, [cm]$	5.566	1.409	1.526	1.744	1.198	0.786	0.679	0.539
$\epsilon \, [cm]$	0.392	-0.197	0.303	0.040	0.045	-0.051	0.095	0.075
$\lvert \epsilon \rvert \, [cm]$	2.569	0.808	0.920	1.189	0.710	0.491	0.488	0.334
$E \, [-]$	0.090	0.106	0.155	0.167	0.135	0.285	0.206	0.301

Finally, we investigated the reasons that cause the outliers identified in the scatter plot for the M2 constituent (see Figure 18). We studied the gauges highlighted in Figure 19a. We found that all those gauges are in areas with bathymetric errors. Specifically, the overpredicted gauges are in the upper section of Merrimack, Piscataqua, and Kennebec rivers in the Gulf of Maine, where topographic databases show increments of the surrounding slopes, but they do not provide water depth values in the channels. We use the NOAA charts to correct the water depth of those rivers, however, we are aware that the charts do not provide the correct representation of bottom river slopes, which might introduce error in the model. The underpredicted gauge is in the Turks and Caicos Islands, where shallow water of the Caicos Banks shown in the satellite image in Figure 19b produces large amplification of the tidal amplitude compared with surrounding areas in the Caribbean. In the model, that area has unrealistically deep-water depths greater than 250 m based on GEBCO 2019, shown in Figure 19c. This does not produce the resonant amplification of the semidiurnal constituents that occurs in reality. Unfortunately, we could not find any other bathymetric database publicly available for this region in order to produce physically correct results.
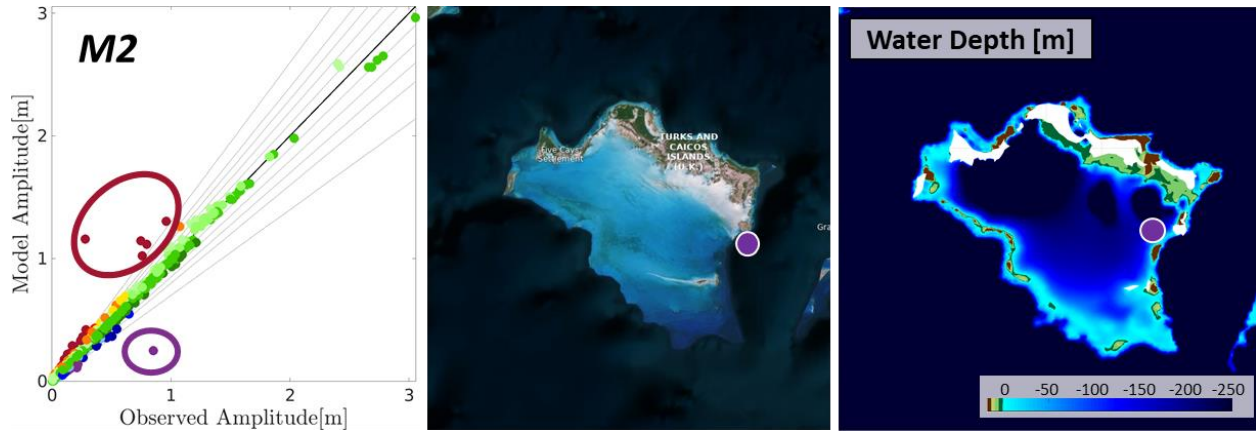
Figure 19: Example of bathymetric errors in the Caicos Bank causing inaccurate tidal results in ECGC_120m_2021_v01 reported by the GESLA station at South Caicos.

We also analyzed the results of the tidal validation with the 786 gauges remaining after deleting the 6 outliers from the original database. Table 3 shows a summary of the statistics when comparing the modeled and observed tidal amplitudes. We notice that all the constituents analyzed improved the coefficient of determination R^2, the absolute mean error $|\epsilon|$, and the root mean square error E. Particularly, the M$_2$ constituent improves the R^2 up to 0.994, with the largest improvement in the P$_1$ constituent that raised up to 0.77. The absolute mean error reduced in 13% for M$_2$, ~7% for N$_2$ and S$_2$, and ~4% for O$_1$, while the rest of constituents reduced it between 0.6 and 2.7%. The root mean square error E, also shows the impact of the gauges poorly resolved due to bathymetric issues. All the constituents reduce its values with the largest impact on the M$_2$ constituent with a drop of 40%, then N$_2$ with 17%, and S$_2$ and O$_1$ with ~14-15%.

Table 3: Summary of statistics when comparing modeled tidal amplitude against a set of 786 gauges, after deleting the outliers showed in Figure 19.

	$M2$	$N2$	$S2$	$K1$	$O1$	$K2$	$P1$	$Q1$
$R^2\ [-]$	0.994	0.988	0.966	0.847	0.933	0.821	0.770	0.663
$y\ [-]$	0.999	0.960	1.030	0.985	0.995	0.896	1.000	1.010
$\sigma\ [cm]$	3.332	1.471	1.294	1.572	1.029	0.776	0.637	0.586
$\epsilon\ [cm]$	0.191	-0.222	0.260	0.050	0.052	-0.041	0.099	0.079
$|\epsilon|\ [cm]$	2.231	0.752	0.856	1.157	0.681	0.484	0.479	0.332
$E\ [-]$	0.054	0.087	0.131	0.151	0.116	0.282	0.195	0.296

We also analyzed the performance of the model comparing the phase of the dominant tidal constituents. Figure 20 shows the comparison against the same 792 tidal gauges shown in Figure 18, classifying the error in constant intervals of 18 degrees. The

figure again shows an excellent model performance in the deep ocean and shelf for all the constituents. Nearshore, the results are in general good, with some local errors. In particular, the semi-diurnal constituents show underpredicted values in eastern Louisiana, an area where the tidal phase changes quickly and is dominated by a well-known amphidromic trough that runs north-south in the central Gulf of Mexico from the Cancun Peninsula to the Mississippi Delta. We believe that the presence of the Gulf Stream will impact the semi-diurnal tidal constituents in the Gulf of Mexico as the main tidal energy inflow is through the Straits of Florida, where the Gulf Stream energetically exits the Gulf. Similarly, some of the underpredicted outliers in the M_2 constituent are in the Gulf of Maine and Bay of Fundy, where the tidal phase changes quickly around Nova Scotia, Canada.
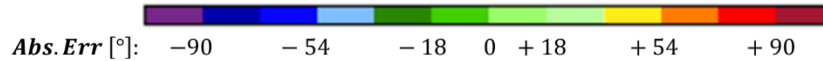
Abs. Err [°]:   −90   − 54   − 18   0 + 18   + 54   + 90
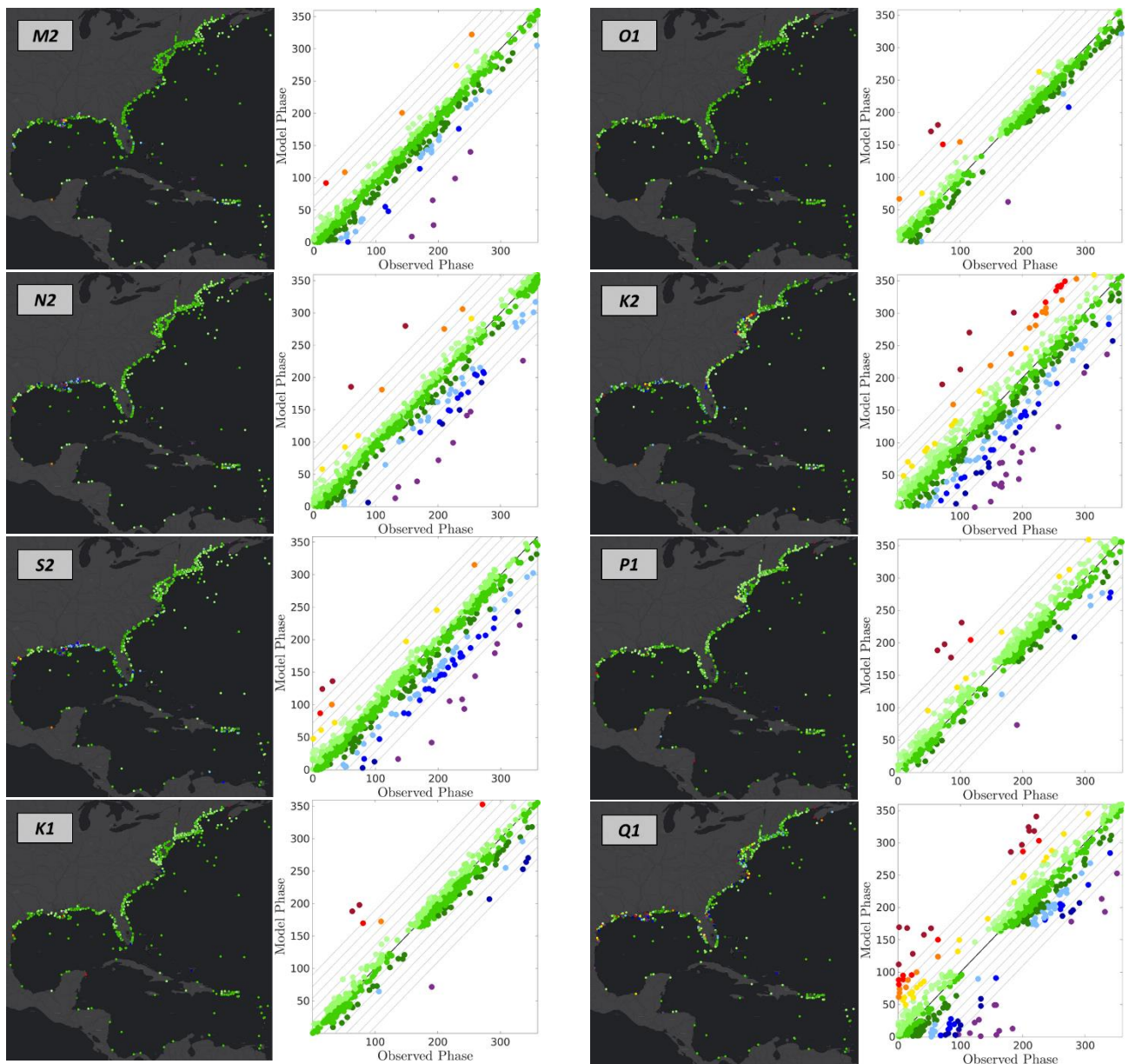
Figure 20: Phase error for the eight dominant astronomical tidal constituents. The statistics are computed based on comparing the results against 792 stations in the deep ocean, shelf, and nearshore.

We also summarized the statistics for the tidal phase in Table 4. Likewise, the tidal amplitude, the general statistics corroborate the excellent performance of the model. The R-squared varies for the tidal phase from 0.883 in Q1 to 0.98 in O1. The mean of the error is always lower than 10 degrees, and the mean of the absolute error reaches 20.429 degrees for Q_1. The normalized root mean square error varies from 0.72 for O_1 to 0.204 for K_2.

Table 4: Summary of statistics when comparing modeled tidal phase against a set of 792 gauges.

	$M2$	$S2$	$N2$	$K2$	$K1$	$O1$	$P1$	$Q1$
$R^2\ [-]$	0.974	0.941	0.971	0.889	0.973	0.980	0.966	0.883
$y\ [-]$	0.960	0.936	0.972	0.947	0.985	0.971	1.004	0.960
σ	16.635°	22.452°	20.524°	31.266°	14.102°	13.046°	16.226°	32.914°
ϵ	-7.213°	-7.498°	-5.515°	-6.135°	-2.237°	-4.494°	2.269°	-5.493°
$\|\epsilon\|$	10.362°	13.357°	11.129°	19.748°	8.012°	8.962°	9.932°	20.429°
$E[-]$	0.111	0.153	0.104	0.204	0.075	0.072	0.086	0.173

7. STORM VALIDATION

We also validated a set of storms that include Gustav (2008), Irene (2011), Sandy (2012), and Irma (2017). We ran a cold start for 18 days with only tidal forcing and then a hot started simulation for the duration of each storm, forcing tides, waves, winds, and atmospheric pressure. We use Oceanweather, INC hindcast wind fields, and a 600-second timestep wave coupling with the SWAN non phase resolving wind wave model. We ran the simulations using the explicit integration time scheme with a 2 second time step. In the analysis of results, we did not consider the first five days of the hot start run, those being considered ramping days.

To simulate storms, we added four nodal attributes to the model: 1) advection_state, 2) surface_directional_effective_roughness_length, 3) surface_canopy_coefficient, and 4) surface_submergence_state. We turned off the advective terms along the line of nodes on the open ocean elevation boundary condition through the advection_state nodal attribute to improve the stability of the model when forcing with waves. We used the surface directional roughness to consider the additional roughness of the land compared with the very smooth ocean. We used the NOAA C-CAP Regional Land Cover database from 2010 (*C-CAP*, 2010) computing the additional roughness in 12 different wind directions. Similarly, we used the surface canopy coefficient to turn off the wind stresses in forested areas. We used the NOAA C-CAP 2016 (*C-CAP*, 2016) to identify all the land cover categorized as "forest". Finally, we added the surface submerge state to ensure that areas enclosed by levees start dry at the beginning of the storm simulation, even though they can have elevations below the sea level.

We analyzed the results by comparing time series and high-water marks against a set of NOAA water level gauges in the areas affected during the storms. We corrected the water levels by computing the vertical difference between the mean of the time series during the tidal simulation and adjusting the time series of the hot start storm simulation. We think this corrects the differences in water levels due to seasonal variations (steric adjustment), and the different vertical datums between the model (MSL) and the NOAA gauges (NAVD88).

Figure 21 shows the results for the simulation of Hurricane Gustav in 2008. Figure 21a shows the maximum water elevation together with the track and magnitude of the storm. The hurricane mostly affected the Louisiana and Mississippi coasts, with a maximum surge of around 3 m along the east side of Louisiana's coast. The figure also shows the errors of the high-water marks for the NOAA water level gauges located between Florida and Texas with data during the storm. Figure 21b shows the scatter plot comparing the observed and modeled high-water mark value as well as a summary of the statistics of the results. Additionally, we point out in Figure 21a the

location and identification number for 4 stations whose hydrographs during the storms are shown in Figure 22.

Almost all the gauges in the area affected show low error rates at calculating the magnitude and timing of the peak, as well as the drop of water levels after the storm. The mean of the errors is only 12 cm, and the absolute mean error is 14 cm. Both significantly lower than the magnitude of the surge that reached over 3 m. The gauge ID8761305 is the largest error in the region, with an underprediction of the maximum water level of approximately 30%. We checked the mesh around the station noticing that the small channels that connect the Lake Borgne with the Mississippi river are resolved but they have obvious bathymetric errors. We think that as the main source of the error, since the shallow water depths in the area are not allowing the correct penetration of the tides prior to the storm and the surge.
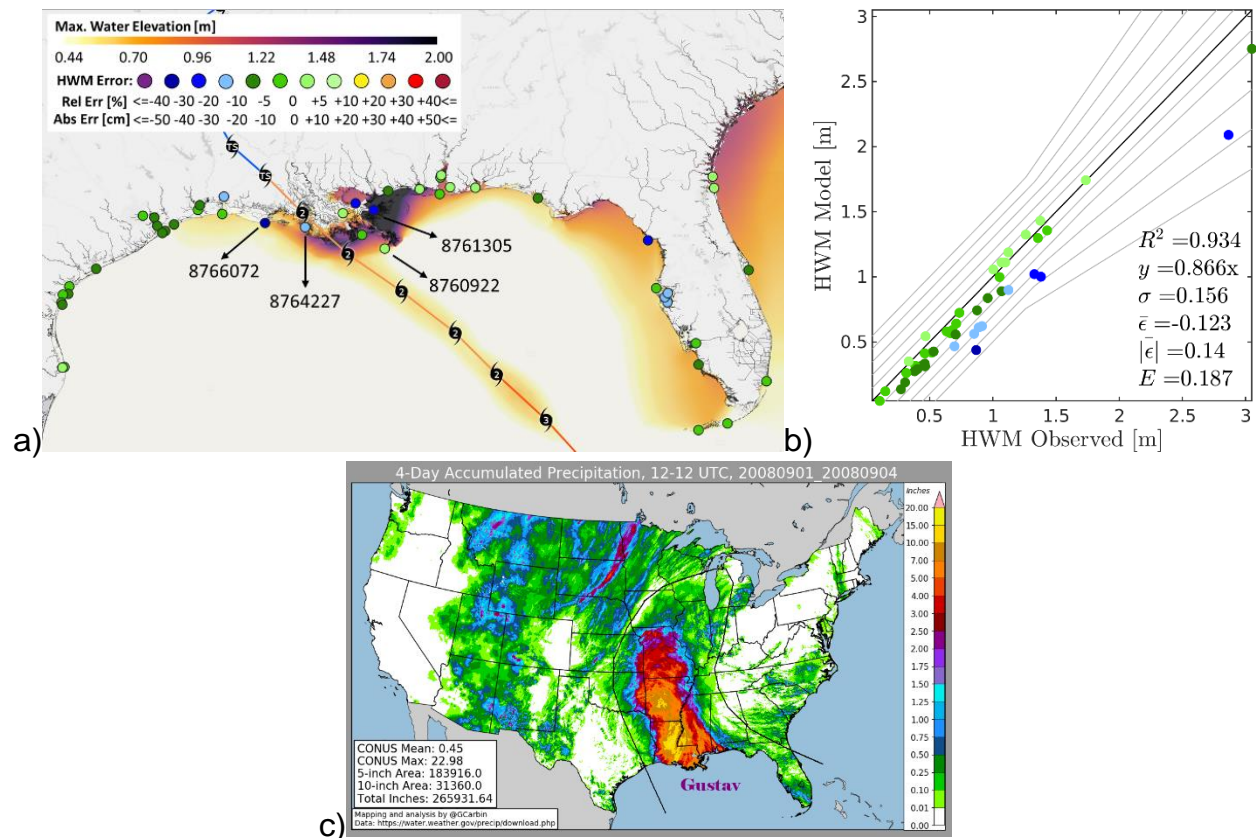

Figure 21: a) Maximum water elevation and comparison of high-water marks at NOAA water level gauges during Hurricane Gustav (2008). B) Scatter plot for high water marks compared against NOAA water level gauges. c) Four-days accumulated precipitation during the hurricane (Source: Weather Prediction Center, NOAA)
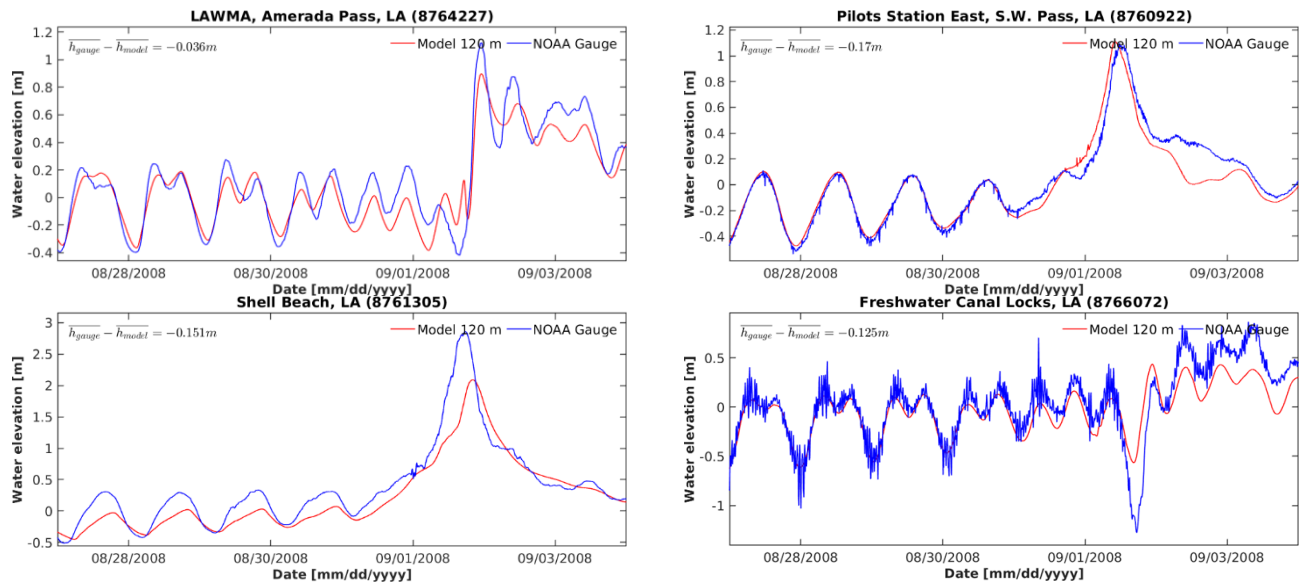
Figure 22: Time series of the water elevation at four NOAA water level gauges during Hurricane Gustav (2008). Their location is shown in Figure 21.

Similar results are shown in Figure 23 and 24 for Hurricane Irene in 2011. The hurricane affected the U.S. East Coast from North Carolina to Massachusetts, showing water levels with a maximum of 2 m approximately and slightly higher values in Long Island Sounds and the back bays in Virginia at the outlet of the Chesapeake Bay. The mean of the errors is only 3.2 cm and the absolute mean error 12 cm. We think that the major underpredictions in the Chesapeake Bay are explained by the missing precipitation that accumulated over 15 inches total in the area. Additionally, we think the baroclinic pressure gradients related to the Gulf Stream have an impact on the nearshore water levels that is not considered in the model. We expect it to push water away from the coast, dropping the levels particularly along the North and South Carolinas coasts. These two additional forces are part of the current research, and they should be addressed in future publications. The time series for four of the gauges are presented in Figure 24. We observe a good representation of the tidal signal, and the peak and trough of water levels due to the winds and surge. The largest error is observed in gauge ID8570283 where the peak is overestimated for about 20 cm for a surge that reached 1.2 m.
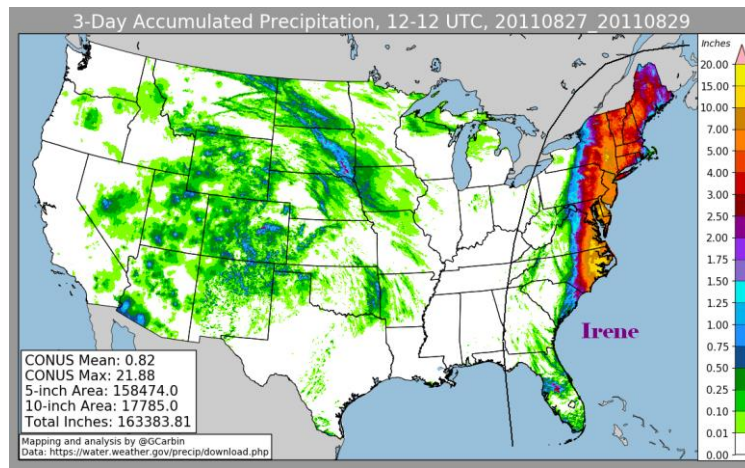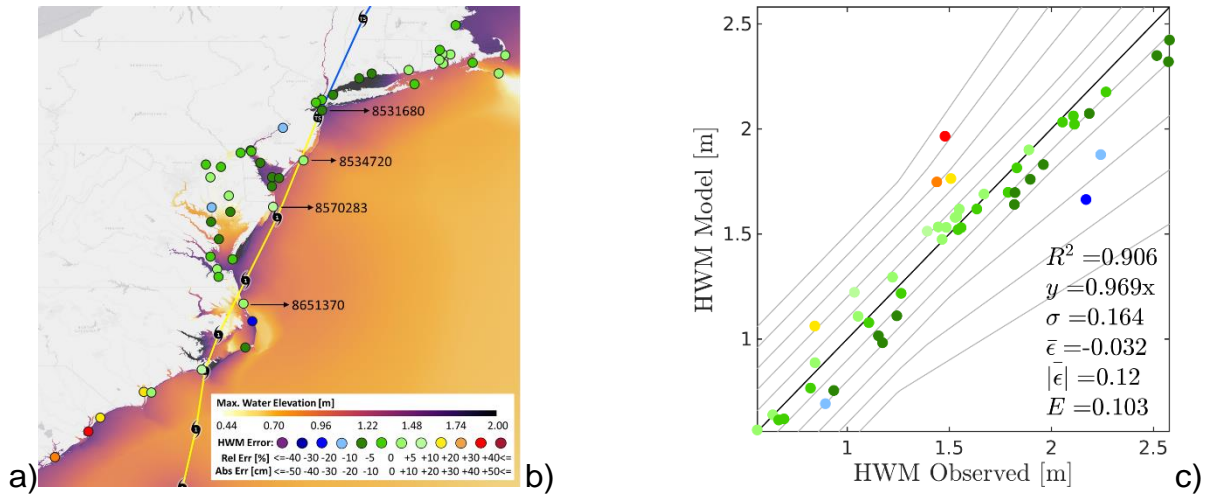
Figure 23: On the left, maximum water elevation and comparison of high-water marks at NOAA water level gauges during Hurricane Irene (2011). On the right, three-days accumulated precipitation during the hurricane (Source: Weather Prediction Center, NOAA)
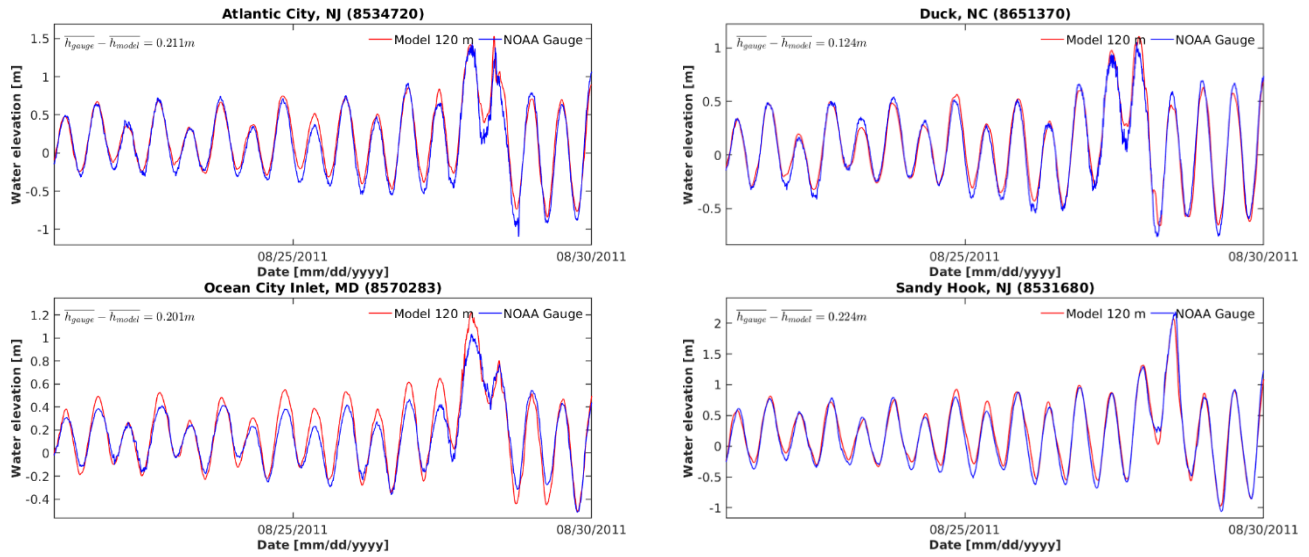
Figure 24: Time series of water elevation at four NOAA water level gauges during Hurricane Irene (2011). Their location is shown in Figure 23.

Figure 25 shows the maximum water levels generated during Hurricane Sandy in 2012. With a large impact along the coast from Maryland to New York, where the water level exceeded 3.5 m. We observe similar magnitude and distribution of the errors as Hurricane Irene, with a mean error of only 4 cm and absolute mean error of 14.2 cm. The most accurate results are found in gauges located North of Delaware, and the underpredictions in Chesapeake. We think that because Sandy's track is much more perpendicular to the coast, we do not observe a strong baroclinic effect along North Carolina's coast. Figure 26 shows that underpredicted gauges as ID8571421 have a good representation of the tidal signal, and that the mismatch that we observed is in the vicinity of the peak of the storm. Similarly, as Hurricane Irene, we think this corresponds with the lack of precipitation in the model, which in this case accumulated over 10 inches near Chesapeake. We also noticed gauge ID 8534720 as the major outlier in the analysis, which is located right along the track of the storm, which means that its error is largely explained by errors in the wind field that are particularly sensitive near the center of the storm.
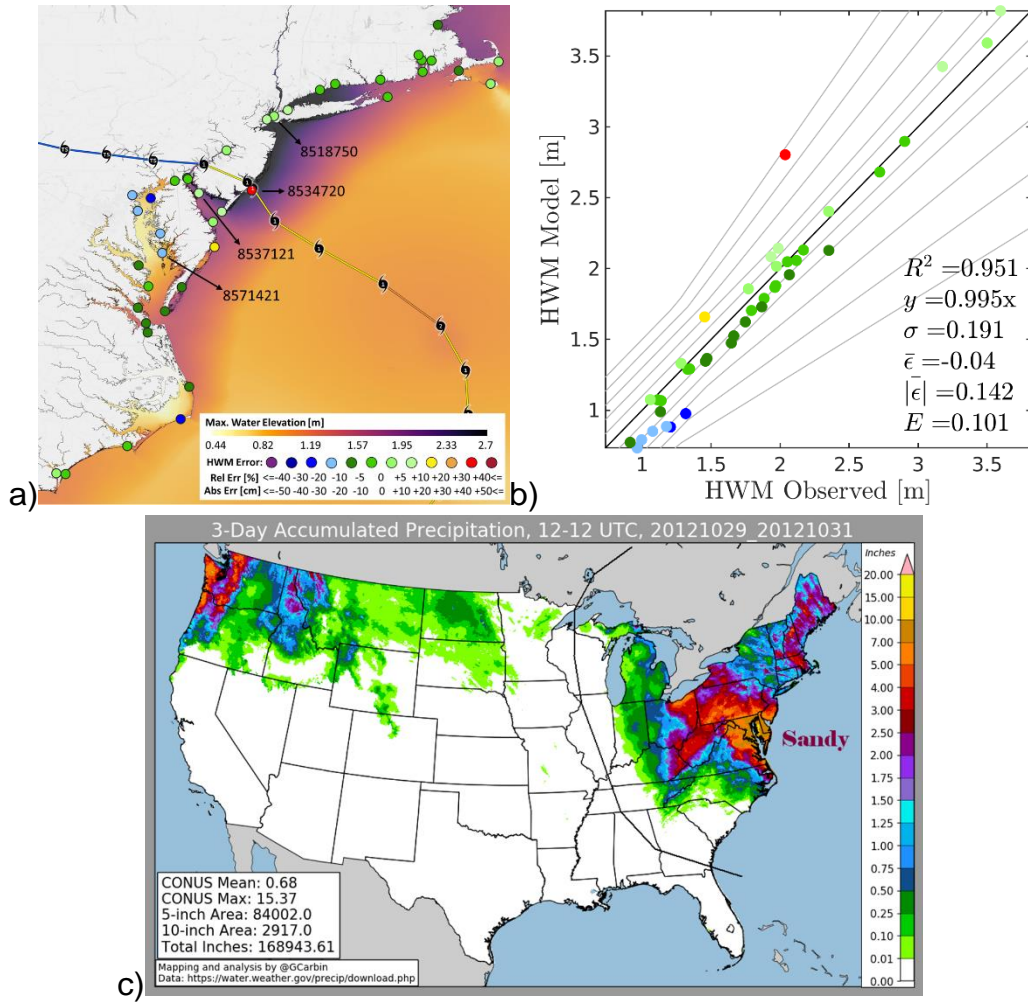
33

Figure 25: On the left, maximum water level elevation and comparison to high-water marks at NOAA water level gauges during Hurricane Sandy (2012). On the right, three-days accumulated precipitation during the hurricane (Source: Weather Prediction Center, NOAA)

Figure 26: Time series of the water elevations at four NOAA water level gauges during Hurricane Sandy (2012). Their location is shown in Figure 25.

Figures 27 and 28 show the results for Hurricane Irma in 2017 which mainly affected the south and west coasts of Florida, dramatically pushing water away from the west coast of Florida. Figure 27b shows a summary of the statistics when comparing against water level NOAA gauges along Florida. We notice that the major errors are in the Keys, where we think there should be a strong influence of the Gulf Stream that is not solved in the model. Figure 28 shows the difference in the hydrographs located along the east coast ID 8723214, and the west coast ID 8726520 and 8725520, with a clear difference in their shape between September 10th and 12nd. We noticed at gauges ID 8723970 and 8725520 that our model does not capture the fast increment of water level after the storm passes, which might be related to the definition of the dissipation parameters in the model.

Figure 27: On the left, maximum water elevation and comparison of high-water mark at NOAA water level gauges during Hurricane Irma (2017). On the right, four-days accumulated precipitation during the hurricane (Source: Weather Prediction Center, NOAA)
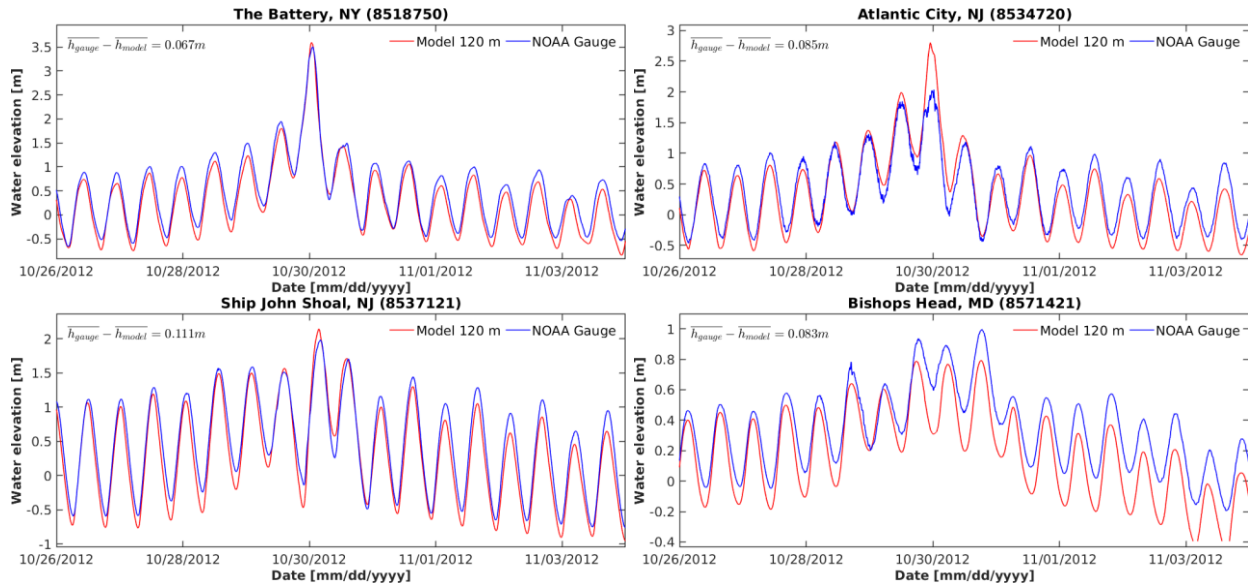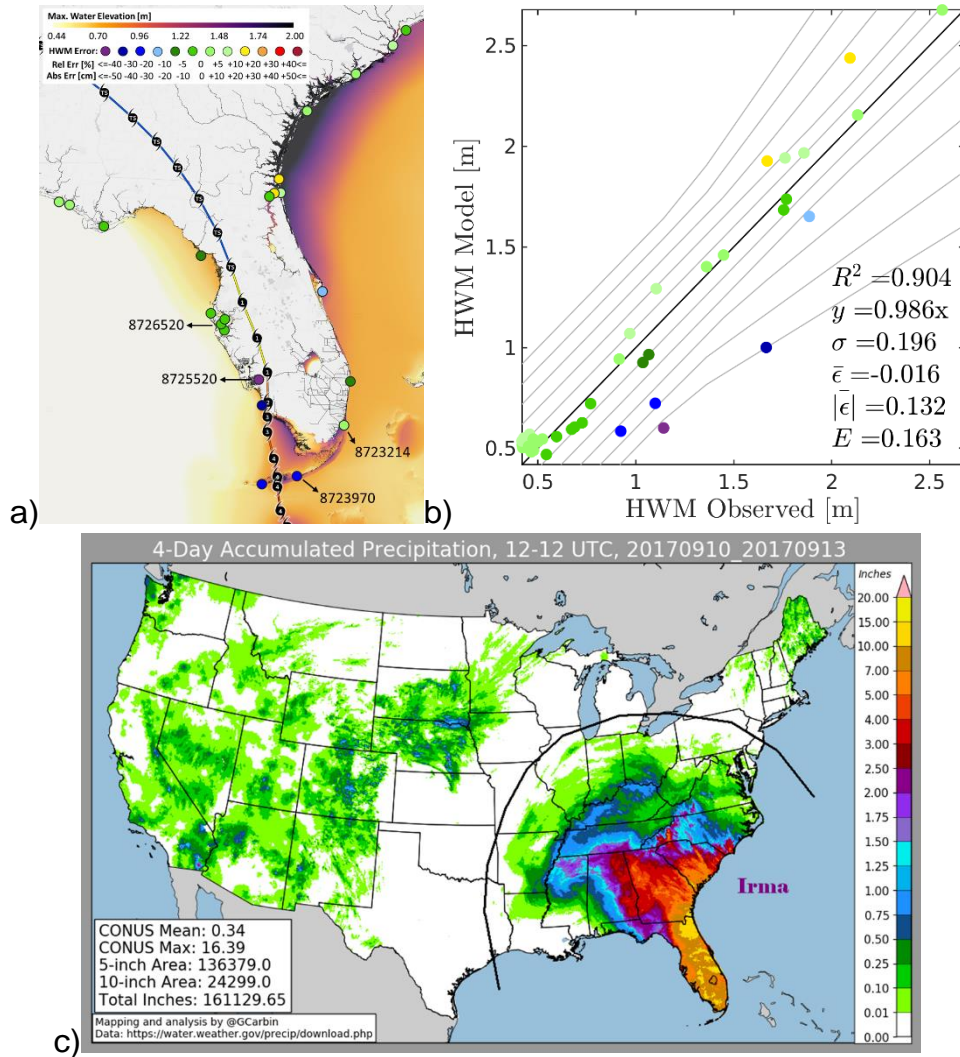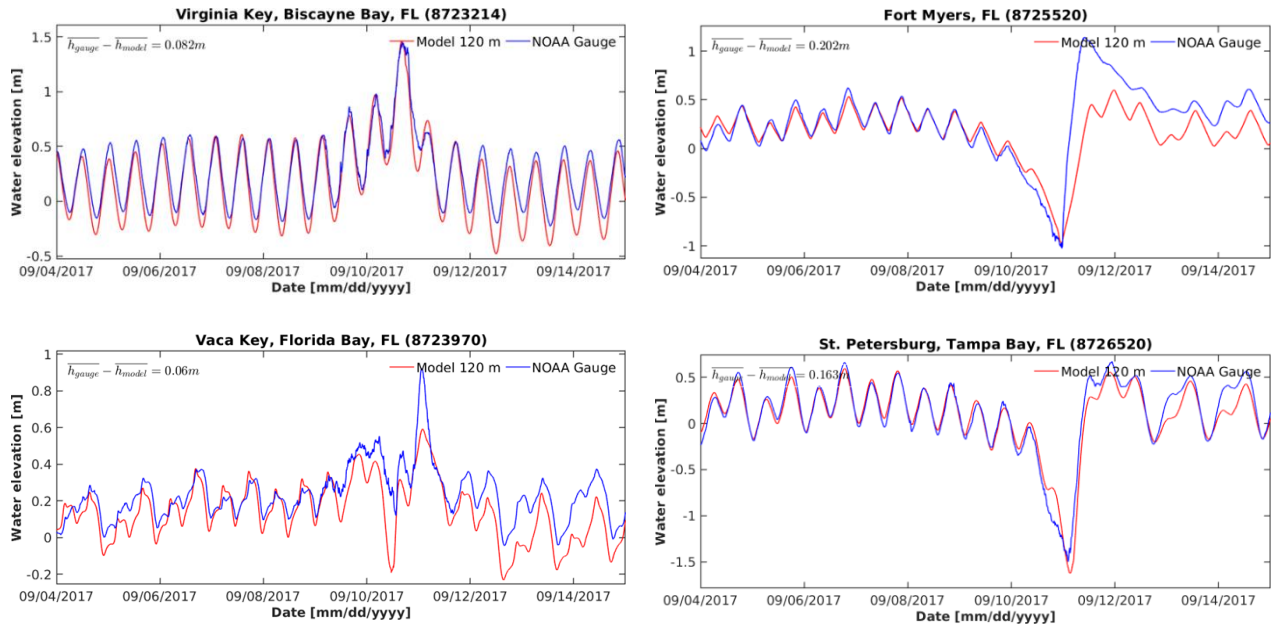
Figure 28: Time series of the water elevation at four NOAA water level gauges during Hurricane Irma (2017). Their location is shown in Figure 2

8. CONCLUSIONS AND FUTURE WORK

This report details the methods, tools, and databases used to implement the new East Coast and Gulf of Mexico storm surge model ECGC_120m_2021_v01. The major advance of this model, compared with its equivalent previous version (Funakoshi et al., 2011, 2013), is the integration of the ocean and the coastal hydrodynamics by accurately resolving the complexity of the inland river network and coastal inlets while keeping the model's computational cost low enough for operational purposes.

The key to solving the connectivity along inland channels was separating the wet and dry portions of the domain through nodes located along the coastline. This allowed us to resolve channels with widths as small as the model's minimum resolution (120 m for ECGC_120m_2021_v01) and incorporate small topographic features such as islands, barrier islands, among others, that play a significant role in the coastal hydrodynamics.

Intending to design a model feasible for operational forecast systems, we used automatic mesh generation tools that allow for an efficient resolution distribution. We used OceanMesh2D because it uses geographic information to define the element size function based on topo-bathymetric features and their geometry. The toolbox receives information from DEMs and coastline, together with a set of user-defined parameters to provide extra resolution where it is required to preserve the accuracy of the simulations, i.e., along steep bathymetric gradients, deep natural and dredged channels, the complex sections of the coastline, among others.

Knowing the relevance of using the most accurate and updated input data for the model implementation, we also describe our efforts in collecting and processing data. We provide details on the data used to define the coastline, the topo-bathymetry, natural and dredged channels, man-made structures, land use, etc.

We validate the model by comparing tides and historical storms results against observations. In the case of tides, the comparison against 792 tidal gauges shows excellent performance of the model in the deep ocean, shelf, and near the coast for the amplitude and phase of the eight major constituents. The tidal validation also highlighted the relevance of accurate bathymetric datasets, showing that the major errors in the tidal prediction occurred in the Turks and Caicos Islands and the Gulf of Maine, where we identified bathymetric errors. In the case of storms, we analyzed our results regarding the high-water marks and hydrographs, comparing them against NOAA water level gauges. We observed accurate results capturing the tides, surges, and drops of water levels previous to and during the storm. However, we noticed discrepancies in the water levels after the storm passes, particularly during

hurricanes Sandy and Irene, which, we think, are caused by baroclinic forces that are not included in this model.

Overall, in this report, we intend to provide guidelines on how to implement basin-to-channel scale models, with the specific details for the East and Gulf of Mexico Coasts of the U.S. We also contribute with a tool that accurately resolves the hydrodynamics of the North Atlantic basin as well as the nearshore region along the East and Gulf of Mexico Coasts of the US, which seeks to replace the previous version the ECGC (Funakoshi et al., 2011, 2013) for operational purposes. We think that this new model generation also sets the basis for our future work focused on advancing towards an integrated hydrologic-ocean model.

REFERENCES

Akrofi, J., Farmer, T., & Nganyi, J. (2016). *Human Settlements on the Coast*. UN Atlas of the Ocean. http://www.oceansatlas.org/subtopic/en/c/114/

Aslaksen, M. L., Blackford, T., Callahan, D., Clark, B., Doyle, T., Engelhardt, W., Espey, M., Gillens, D., Goodell, S., Graham, D., Hawken, B., Hippenstiel, R., Jennings, D., Kerns, C., Livengood, C., Marmalyukov, R., Matula, S., Pakai, R., Sloan, C., …

Bashant, K. (2019). *Scope of Work for Shoreline Mapping Under the NOAA Coastal Mapping Program* (Issue 15).

C-CAP Regional Land Cover and Change. (2010). Coastal Change Analysis Program (C-CAP) Regional Land Cover. www.coast.noaa.gov/htdata/raster1/landcover/bulkdownload/30m_lc/

C-CAP Regional Land Cover and Change. (2016). Coastal Change Analysis Program (C-CAP) Regional Land Cover. www.coast.noaa.gov/htdata/raster1/landcover/bulkdownload/30m_lc/

Colle, B. A., Booth, J. F., & Chang, E. K. M. (2015). A Review of Historical and Future Changes of Extratropical Cyclones and Associated Impacts Along the US East Coast. *Current Climate Change Reports*, *1*(3), 125–143. https://doi.org/10.1007/S40641-015-0013-7/FIGURES/13

Compilation, G. G. (2019). *GEBCO 2019 Grid*. https://doi.org/10.5285/836f016a-33be-6ddc-e053-6c86abc0788e

Dronkers, J. (1986). Tidal asymmetry and estuarine morphology. *Netherlands Journal of Sea Research*, *20*(2–3), 117–131. https://doi.org/10.1016/0077-7579(86)90036-0

Egbert, G. D., & Erofeeva, S. Y. (2002). Efficient inverse modeling of barotropic ocean tides. *Journal of Atmospheric and Oceanic Technology*, *19*(2), 183–204. https://doi.org/10.1175/1520-0426(2002)019<0183:EIMOBO>2.0.CO;2

Engwirda, D. (2014). Locally optimal Delaunay-refinement and optimization-based mesh generation. *Ph.D. Thesis*, 204.

Engwirda, D. (2017). JIGSAW-GEO (1.0): Locally orthogonal staggered unstructured grid generation for general circulation modelling on the sphere. *Geoscientific Model Development*, *10*(6), 2117–2140. https://doi.org/10.5194/gmd-10-2117-2017

Funakoshi, Y., Feyen, J., Aikman, F., Tolman, H., van der Westhuysen, A., Chawla, A., Rivin, I., & Taylor, A. (2011). Development of Extratropical Surge and Tide Operational Forecast System (ESTOFS). *Estuarine and Coastal Modeling*, *38*, 201–212. https://doi.org/10.1061/9780784412411.00012

Funakoshi, Y., Feyen, J., Aikman III, F., van der Westhuysen, A., & Tolman, H. (2013). *NOAA Technical Report Nos Cs 32 The: The Extratropical Surge and Tide Operational Forecast System (ESTOFS) Atlantic Implementation and Skill Assessment* (Issue October).

Galperin, B., & Mellor, G. L. (1990). A time-dependent, three-dimensional model of the Delaware Bay and River system. Part 2: Three-dimensional flow fields and residual circulation. *Estuarine, Coastal and Shelf Science*, *31*(3), 255–281. https://doi.org/10.1016/0272-7714(90)90104-Y

Graham, D. (2020). NOAA'S Continually Updated Shoreline Product (CUSP). In *Coastal Coupling Community of Practice Webinar Series*. NOAA.

Greenberg, D. A., Dupont, F., Lyard, F. H., Lynch, D. R., & Werner, F. E. (2007). Resolution issues in numerical models of oceanic and coastal circulation. *Continental Shelf Research*, *27*(9), 1317–1343. https://doi.org/10.1016/J.CSR.2007.01.023

Knutson, T., McBride, J., Chan, J., Emanuel, K., Holland, G., Landsea, C., Held, I., Kossin, J., Srivastava, A. K., & Sugi, M. (2010). Tropical cyclones and climate change. *Nature Geoscience*, *3*, 157–163. https://doi.org/10.1038/NGEO779

Kossin, J. P. (2018). A global slowdown of tropical-cyclone translation speed. *Nature*, *558*(7708), 104–107. https://doi.org/10.1038/s41586-018-0158-3

Luettich, R. A., Westerink, J. J., & Scheffner, N. W. (1992). ADCIRC: An Advanced Three-Dimensional Circulation Model for Shelves Coasts and Estuaries, Report 1: Theory and Methodology of ADCIRC-2DDI and ADCIRC-3DL, Dredging Research Program Technical Report DRP-92-6. In *Coastal Engineering Research Center (U.S.), Engineer Research and Development Center (U.S.).* (Issue 32466, pp. 1–137).

Luettich, R., & Westerink, J. (2004). *Formulation and Numerical Implementation of the 2D / 3D ADCIRC Finite Element Model Version 44. XX* (R. Luettich, Ed.).

Luettich, R., & Westerink, J. (2018, April 8). *ADCIRC User's manual v53*. https://adcirc.org/home/documentation/users-manual-v53/input-file-descriptions/

Masson-Delmotte, V., Zhai, P., Pirani, A., Connors, S., Péan, C., Berger, S., Caud, N., Chen, Y., Goldfarb, L., Gomis, M., Huang, M., Leitzell, K., Lonnoy, E., Matthews, J., Maycock, T., Waterfield, T., Yelekçi, O., Yu, R., & Zhou, B. (2021). *IPCC, 2021: Climate Change 2021: The Physical Science Basis. Contribution of Working Group I to the Sixth Assessment Report of the Intergovernmental Panel on Climate Change.* https://www.ipcc.ch/report/ar6/wg1/downloads/report/IPCC_AR6_WGI_Full_Report.pdf

Masters, J. (2007, November 28). 2017 U.S. Hurricane Damage Estimate of $206.6 Billion: Highest on Record. *Weather Underground*. https://www.wunderground.com/cat6/2017-us-hurricane-damages-206-billion-highest-record

Molines, J. M., Fornerino, M., & le Provost, C. (1989). Tidal spectroscopy of a coastal area: observed and simulated tides of the Lake Maracaibo system. *Continental Shelf Research*, *9*(4), 301–323. https://doi.org/10.1016/0278-4343(89)90036-8

Moon, I. J., Kim, S. H., & Chan, J. C. L. (2019). Climate change and tropical cyclone trend. *Nature*, *570*(7759), E3–E5. https://doi.org/10.1038/s41586-019-1222-3

National Oceanic and Atmospheric Administration (NOAA), N. G. S. (2021). *NOAA's Continually Updated Shoreline Product.* https://shoreline.noaa.gov/data/datasheets/cusp.html

NOAA. (2013). National coastal population report: Population trends from 1970 to 2010. *NOAA State of the Coast Report Series*, 22.

NOAA Office of Coast Survey. (2021). *NOAA Chart Locator*. Retrieved November 10, 2021, from https://www.charts.noaa.gov/InteractiveCatalog/nrnc.shtml

NOAA's Ocean Service, C. S. C. (CSC). (1998). *NOAA's Medium Resolution Digital Vector Shoreline (1998) for the Contiguous United States*. http://csc.noaa.gov/htdata/Shoreline/us_medium_shoreline.zip

Pringle, W. J., Wirasaet, D., Roberts, K. J., & Westerink, J. J. (2021). Global storm tide modeling with ADCIRC v55: Unstructured mesh design and performance. *Geoscientific Model Development*, *14*(2), 1125–1145. https://doi.org/10.5194/gmd-14-1125-2021

Pringle, W. J., Wirasaet, D., Suhardjo, A., Meixner, J., Westerink, J. J., Kennedy, A. B., & Nong, S. (2018). Finite-Element barotropic model for the Indian and Western Pacific Oceans: Tidal model-data comparisons and sensitivities. *Ocean Modelling*, *129*, 13–38. https://doi.org/10.1016/J.OCEMOD.2018.07.003

Reidmiller, D. R., Avery, C. W., Easterling, D. R., Kunkel, K. E., Lewis, K. L. M., Maycock, T. K., & Stewart, B. C. (2018). Impacts, Risks, and Adaptation in the United States: Fourth National Climate Assessment, Volume II. In *Fourth National Climate Assessment: Vol. II*. https://doi.org/10.7930/NCA4.2018

Roberts, K. J., & Pringle, W. J. (2018). *OceanMesh2D: User guide - Precise distance-based two-dimensional automated mesh generation toolbox intended for coastal ocean/shallow water flow models. September 2020*, 40. https://doi.org/10.13140/RG.2.2.21840.61446/2

Roberts, K. J., Pringle, W. J., & Westerink, J. J. (2019). OceanMesh2D 1.0: MATLAB-based software for two-dimensional unstructured mesh generation in coastal ocean modeling. *Geoscientific Model Development*, *12*(5), 1847–1868. https://doi.org/10.5194/gmd-12-1847-2019

Roberts, K. J., Pringle, W. J., Westerink, J. J., Contreras, M. T., & Wirasaet, D. (2019). On the automatic and a priori design of unstructured mesh resolution for coastal ocean circulation models. *Ocean Modelling*, *144*. https://doi.org/10.1016/j.ocemod.2019.101509

Tozer, B., Sandwell, D. T., Smith, W. H. F., Olson, C., Beale, J. R., & Wessel, P. (2019). Global Bathymetry and Topography at 15 Arc Sec: SRTM15+. *Earth and Space Science*, *6*(10), 1847–1864. https://doi.org/10.1029/2019EA000658

USACE. (2021-a). *National Levee Database*. Retrieved November 10, 2021, from https://levees.sec.usace.army.mil/#/

USACE. (2021-b). *USACE Hydrographic Surveys (eHydro)*. Retrieved November 10, 2021, from https://www.arcgis.com/apps/dashboards/4b8f2ba307684cf597617bf1b6d2f85d

USACE Hydrographic Surveys. (2021). Retrieved November 10, 2021, from https://www.arcgis.com/apps/dashboards/4b8f2ba307684cf597617bf1b6d2f85d

USGS. (2001). *National Hydrography Dataset (NHD)*. https://doi.org/10.3133/

70046927

Weatherall, P. A., Sandwell, D. T., Arndt, J. E., Bringensparr, C., Dorschel, B., Ferrini, V., Giulivi, C. F., Hehemann, L., Jakobsson, M., Johnson, P., Ketter, T., Lamarche, G., Mackay, K., Martin, T. v, Mayer, L. A., Mohammad, R., Nitsche, F. O., Snaith, H., Steinmetz, T., & GEBCO Bathymetric Compilation Group 2019. (2019). The GEBCO_2019 Grid - a continuous terrain model of the global oceans and land. In *Published Data Library (PDL)*. British Oceanographic Data Centre. https://doi.org/10.5285/836f016a-33be-6ddc-e053-6c86abc0788e